

MONASH UNIVERSITY

HONOURS THESIS

Thin oxides in graphene devices

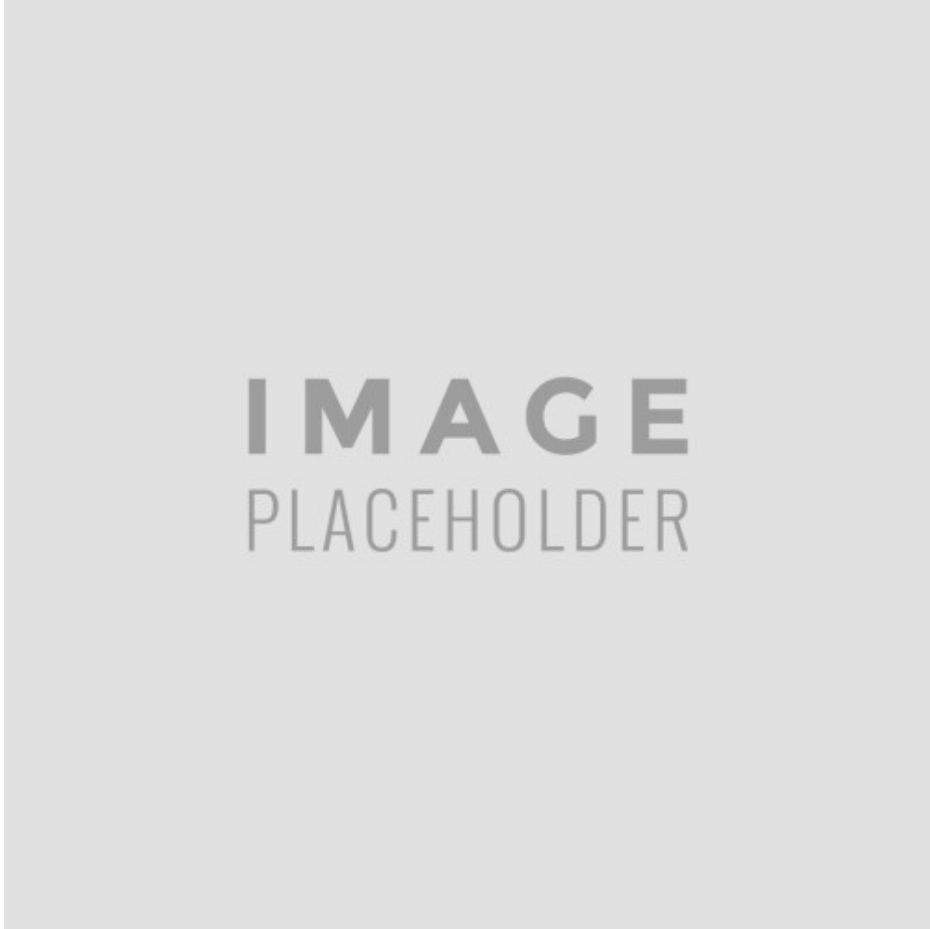


IMAGE
PLACEHOLDER

Supervisors:

Michael Fuhrer
Semonti Bhattacharyya

Physics Honours, Monash University
Student ID: 24121843

Abstract

I present a review of the use of graphene in electronic devices, both in its shortfalls and exciting properties. The electronic structure is detailed, along with various scattering sources that affect electron transport and ultimately the goal of room temperature, electronic devices. Considering heterostructures and the use of other materials to enhance graphene, I discuss the potential use of hafnium dioxide, and other oxides, as an excellent gate dielectric material for potential use in graphene field-effect devices.

Contents

Abstract	1
Foreword	4
1 Introduction	5
1.1 Preface	5
1.2 Transistors - the field effect	5
1.2.1 Conductivity in FETs	5
1.2.2 Mobility in FETs	5
1.3 Graphene	5
1.3.1 Electronic properties	5
1.3.1.1 Hybridisation	6
1.3.1.2 Electronic dispersion	6
1.3.1.3 Charged puddling	6
1.4 Transport and scattering in graphene	6
1.4.1 Charged impurities	6
1.4.2 Phonon scattering	6
1.4.3 Dielectric screening	6
1.4.3.1 Charge screening	6
1.4.3.2 Fine structure constant	6
1.4.3.3 Tuning the fine structure constant	6
1.4.3.4 High κ materials	6
1.4.4 Remote phonon scattering	6
1.5	6
2 Experimental techniques	7
2.1 Fabrication	7
2.1.1 Graphene	8
2.1.2 Chemical vapour deposition graphene	8
2.1.3 Exfoliation of graphene	9
2.1.4 Lithography	10
2.1.4.1 Spin coating photoresists	10
2.1.4.2 Exposure	11
2.1.4.3 Developers	12
2.1.4.4 Contact pad dimensions	12
2.1.5 UV Ozone surface preparation	13
2.1.6 Deposition	13
2.1.6.1 Oxide Protection	14
2.1.7 Lift-off	14
2.1.7.1 Ultrasonication	14
2.1.8 Argon/Hydrogen Annealing	15
2.1.9 PCB board mounting	15

2.1.10	Oxide stamping	16
2.2	Measurement techniques	16
2.2.1	Four probe measurements	17
2.2.1.1	Sourcemeters	18
2.2.1.2	Lock-in amplifiers	18
2.2.2	Probe station	19
2.2.2.1	Vacuum	20
2.2.2.2	Temperature control	20
2.2.2.3	Static Discharge	20
2.2.2.4	Probes	21
3	Characterisation of graphene	22
3.1	Raman spectroscopy	22
3.1.1	Raman in graphite	22
3.1.2	Raman in graphene	22
3.2	Optical microscopy	24
3.2.1	Contrast imaging	25
4	Electrical measurements of pristine graphene	27
4.1	Resistance to resistivity	27
4.2	Gate dependent conductivity	28
4.2.1	Finding the geometric factor of CVD graphene	29
4.3	Temperature & gate dependent conductivity	31
4.3.1	V_G R mobility	32
4.3.2	Temperature dependent conductivity	33
4.3.2.1	EXF06 - Exfoliated graphene	33
4.3.3	hBN transfer	36
5	Thin oxides	37
5.1	Printing	37
5.1.1	Al_2O_3	37
5.1.2	SnO & Bi_2O_3	39
5.2	Smearing Ga_2O_3	41
5.2.1	Devices	41
6	Conclusion	42
6.1	Future direction	42
6.2	Concluding remarks	42
List of Figures		43
List of Tables		45
7 Bibliography		46
Appendices		49
A Gate voltage conductivity fits		50
A.1	EXF06 Fits	50
B Theoretical electronic transport in graphene		58

Foreword

This thesis serves the purpose presenting the conclusions of my research into thin oxides on graphene. I will be arguing , and how that fits into a bigger picture of materials science and particular applications.

In chapter 1, I will outline what I hope to achieve in this project. I begin by discussing the theoretical properties of graphene and why it has attracted so much interest as an electronic material. I will also describe some challenges facing new computing technologies, including the use of dielectrics, and how my work contributes to realising solutions to new generations of this technology. I will outline a theoretical and experimental summary of the results to date seen in introducing dielectrics to graphene.

In chapter 2, I describe the various ways of producing and identifying graphene in lab use, and the characterisations I have conducted. This will include our use of atomic force microscopy (AFM), optical microscopy and Raman spectroscopy.

I will then describe the devices and measurements I have made in chapter 3. This will regard connections to devices, which allow the measurements I have perform, and the processes used to fabricate our devices. I have made graphene devices using lithography and evaporation methods, to create electrical contacts. I will also describe the oxides I have investigated in this chapter, and the methods I have used to transfer them.

In chapter 4 I will present the data and results from my measurements of the respective devices which will be placed on SiO_2 . The results to here will be compared alongside data after stamping the same devices with thin oxides in chapter 5.

Chapter 1

Introduction

1.1 Preface

The mechanical exfoliation of atomically thin materials in 2004 sparked a flurry of research into many materials with unique properties. Graphene, the first of these, rose to prominence in research and has begun finding applications in industrial contexts.

Materials that are two dimensional restrict the movement of electrons to a plane. Because of this, these materials exhibit unique electronic properties. A clear example of this is a hexagonal lattice of carbon atoms, or graphene, which gives rise to a 'dirac' point in the band structure (see section 1.3.1.2).

1.2 Transistors - the field effect

1.2.1 Conductivity in FETs

1.2.2 Mobility in FETs

1.3 Graphene

1.3.1 Electronic properties

Why is it a good conductor?

1.3.1.1 Hybridisation

1.3.1.2 Electronic dispersion

1.3.1.3 Charged puddling

1.4 Transport and scattering in graphene

1.4.1 Charged impurities

1.4.2 Phonon scattering

1.4.3 Dielectric screening

1.4.3.1 Charge screening

1.4.3.2 Fine structure constant

1.4.3.3 Tuning the fine structure constant

1.4.3.4 High κ materials

1.4.4 Remote phonon scattering

1.5

Chapter 2

Experimental techniques

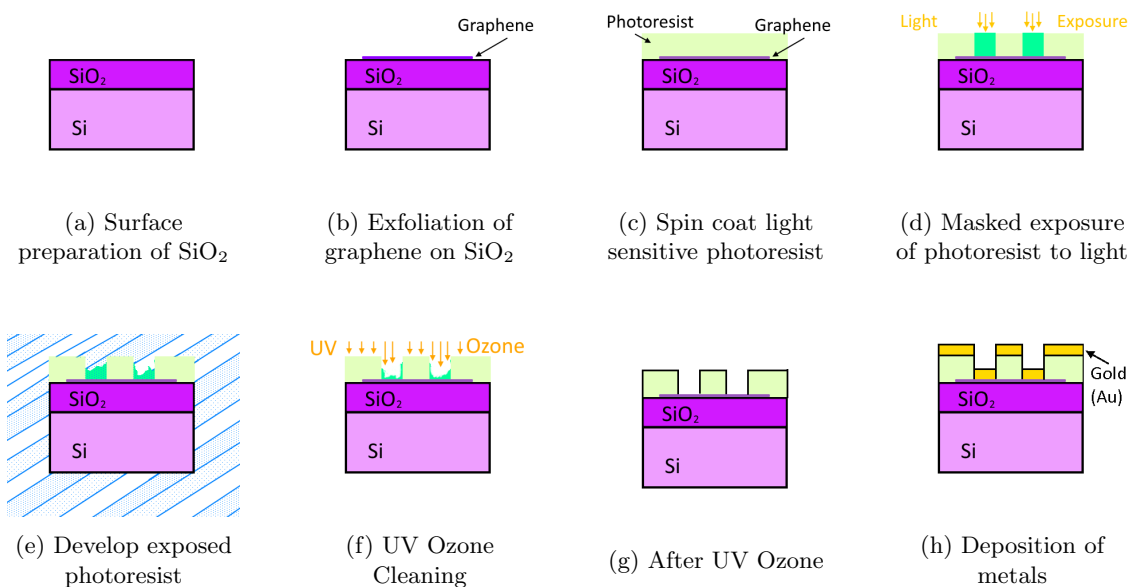
Two aspects are involved in performing electronic measurements of materials, namely fabrication and measurement techniques.

Physical devices containing graphene need to be fabricated to allow measurements to take place. This primarily deals with the production of materials (graphene, oxides) and the processes to develop electrically connectable devices. Some of the tools and techniques used include lithography, electron beam evaporation, and etching. The processes used in this project are detailed in section 2.1.

To measure the electronic transport properties of graphene, particular experimental methods and procedures are required to control the environment and obtain useful data. Section 2.2 primarily deals with the operation of the experimental apparatus used to measure the electronic properties of graphene.

2.1 Fabrication

To create graphene devices where we can measure the electronic properties referenced in sections 1.2 and 1.3.1, a variety of steps need to be taken in order to probe electronic flow. Figure 2.1 describes the general process for exfoliated graphene (see section 2.1.3), the bulk of the devices.



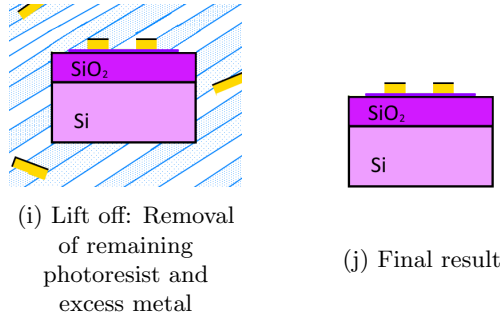


Figure 2.1: Device fabrication process from exfoliated graphene to a FET device.

2.1.1 Graphene

Since the realisation of graphene in 2004^[1], much research has been focused to finding efficient ways of producing large amounts of graphene^[2]. The first samples studied were created using mechanical exfoliation (section 2.1.3)^[3]. These samples typically exhibit better electronic properties than those produced by other methods, and allow for higher sensitivity in measurements. However production is painstaking and produces very small samples. Since 2008/2009, CVD (section 2.1.2) of carbon to create graphene films has provided another prominent method to produce large films for industrial scale applications. In particular, growth of graphene on copper sheets^[4] has been a reliable way producing these large uniform sheets.

There are other methods not used in this thesis, such as epitaxial growth of graphene via SiC uses heating to boil off silicon atoms to form a layer of graphene on its surface^[5;6].

2.1.2 Chemical vapour deposition graphene

Graphene can be growth via chemical vapour deposition, resulting in particularly large uniform sheets when grown on copper^[4]. This is a widely used method of producing readily available graphene. Graphene produced in this fashion needs to be transferred onto an insulating layer of oxide (gate dielectric) on conducting silicon (gate electrode) to create a gated structure. Alternatively, a top gate can be fabricated by deposition a dielectric material followed by creating metal electrodes on top of the graphene. We have used the transfer method onto Si/SiO₂ which has a few problems, in that will introduce some cracks, folding and wrinkling disorder. This is preferable because comparisons can be directly made between exfoliated samples on Si/SiO₂ and CVD transfers.

To achieve this, a process^[7] using polymethyl methacrylate (PMMA) is used to 'wet transfer' CVD graphene onto a SiO₂ wafer with pre-deposited Au pads, from a masked e-beam deposition (see section 2.1.6). Copper grown CVD graphene, covered by a thin layer of PMMA, is placed in an ammonium persulfate solution, dissolving the copper. Hydrophobic graphene and PMMA floats on the surface, and allows substrates dipped into the solution to collect the graphene/PMMA stack from

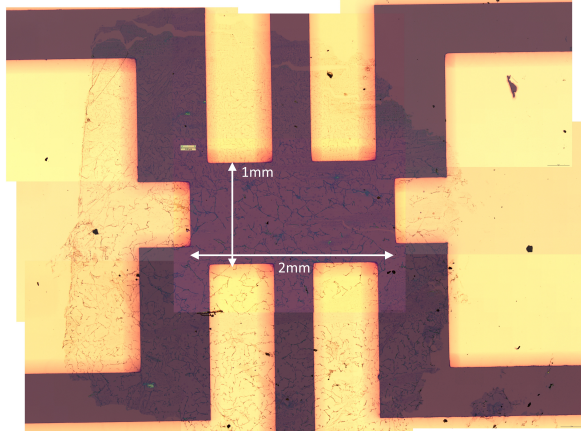


Figure 2.2: CVD graphene grown on Cu transferred onto SiO₂ and Au pads. The contrast differences due to the autoexposure of the camera software.

beneath. After the transfer is complete, the sample is soaked in PG remover to clean off PMMA. PG remover is solvent stripper, efficiently removing PMMA and other resist films on a variety of substrates^[8]. PG remover can also be used as a liftoff solvent, which will be discussed later in section 2.1.7. An example device of transferred CVD graphene is shown in fig. 2.2.

We seldom used this technique to produce graphene devices, due to issues in creating such large area coverage with liquid metal oxide synthesis (refer to chapter 5). Another issue is the lack of geometric definition, however this can be found, as described in section 4.2.1.

2.1.3 Exfoliation of graphene

Exfoliation in materials refers to the cleaving thin layers (or leaves) off a larger sample, and acquiring them onto the substrate. We exfoliate graphene onto Si/SiO₂ wafers. Generally exfoliation involves pressing tape/surfaces against a bulk crystal (such as highly orientated pyrolytic graphite (HOPG), Kish graphite, or natural graphite). Due to van der Waals interactions, layers of graphite are transferred to the desired surface. By repeated peeling of the same tape, a thin coverage can be obtained and then transferred onto substrates, such as SiO₂. Exfoliation can take a variety of forms, from Geim's method^[3], to directly applying scotch tape to HOPG and then pressing against SiO₂, before peeling the tape off.

Huang *et al.* investigated a reliable method of exfoliation to produce large area and high quality samples^[9], which has been widely cited. Tape with graphite flakes is brought into contact with a silicon dioxide wafer, and an annealing process of heating the tape and wafer for 2-5 minutes at $\sim 100^{\circ}\text{C}$ on a conventional lab hot plate is used. After allowing cooling to room temperature, the tape is removed. They find under optical microscopy that graphene flakes with uniform thickness routinely range from $\sim 20 \mu\text{m}$ to above $100 \mu\text{m}$. In this context, annealing is expected to increase adhesion due to the remove of gas molecules trapped between SiO₂ and graphite.

The following steps make up the process of exfoliation we optimised:

1. (Optional) Use a plasma ashing/etcher with an argon/oxygen plasma to the clean surface of SiO₂. This can increase the adhesion between graphene and the surface by removing organic absorbates^[9]. Alternatively, clean wafers of Si/SiO₂ in acetone, tilted in an ultrasonic bath for 30s. Repeat the same in isopropanol, before rinsing in ethanol and drying with N₂ gas.
2. Cleave a layer of HOPG graphite by using scotch tape to peel off a thick film.
3. Use a secondary piece of scotch tape to exfoliate a thinner layer off master tape. Ensure good coverage by reattaching a couple times.
4. Attach Si/SiO₂ wafers to graphite covered areas of secondary tape. The SiO₂ face should be contacting the graphite.
5. Attach the tape and wafers firmly to a glass slide, before using a tissue/cotton-bud to press the surface of the tape into the wafer.
6. Place glass slide on a hotplate at 100°C for two minutes, before removing and cooling for two minutes.
7. Slowly peel tape at an acute angle from the glass slide, roughly at 6s per cm over the wafer.

We found success can depend on the particular HOPG crystal used; given we tried cleavage using ZYA and ZYB quality crystals and had repeated failure to obtain any significant sheets of graphene larger than $4 \mu\text{m}$ in dimension. Changing to a new ZYA crystal provided immediate results using the same process, with the observation of many wafers per substrate larger than $10 \mu\text{m}$ in dimension.

After exfoliation, graphene was identified under a 20x microscope lens, by raster scanning across each wafer to identify graphene samples of a usable size in photolithography. Typically to make a device using photolithography, a sample of graphene required a minimum of $8 \mu\text{m}$ in its longest lateral dimension to be useful.

2.1.4 Lithography

Lithography can be used to create polymer structures that allow the deposition of desired material in 2D geometries. This is used to create electrical contacts onto graphene. This process and the adjustments made for fabricating our devices are described in this section.

Lithography typically consists of three main steps.

1. Spin coating - covering a sample with a uniform layer of polymer, and baking it on.
2. Exposure - The polymer undergoes chemical changes to its properties when exposed to particular wavelengths of light. This differentiates exposed areas to those unexposed.
3. Developer solution - developer solution removes intended areas of photoresist to create structures.

2.1.4.1 Spin coating photoresists

A spin coater is used to deposit thin films of materials. A vacuum holds a sample on the spinner, before drops of photoresist are introduced to the sample, which is then spun for a predetermined time and sometime to achieve a uniform thickness of covering photoresist. Baking on a hotplate follows to set the photoresist layer on the sample.

Photoresists vary in their spinning thickness, but also their exposure rates. Positive photoresists dissolve in particular developer solutions when exposed to light, while negative photoresists dissolve if not exposed to light. We have only used positive photoresists, as we have primarily been creating structures for deposition, and not etching material where you want the bulk of the wafer exposed.

HMDS & AZ-1512HS Initially devices were fabricated using the AZ-1512HS polymer, with the additional use of hexamethyldisilazane (HMDS) as an adhesion promoter between SiO_2 and AZ-1512HS. Devices were spun initially for 10 s at 1000 rpm, before being spun between 2000 and 3000 rpm for 30 s, per resist layer. This leaves a thickness of 1.7 μm to 1.39 μm ^[10]. Devices were then baked at 100 °C for 1 minute.

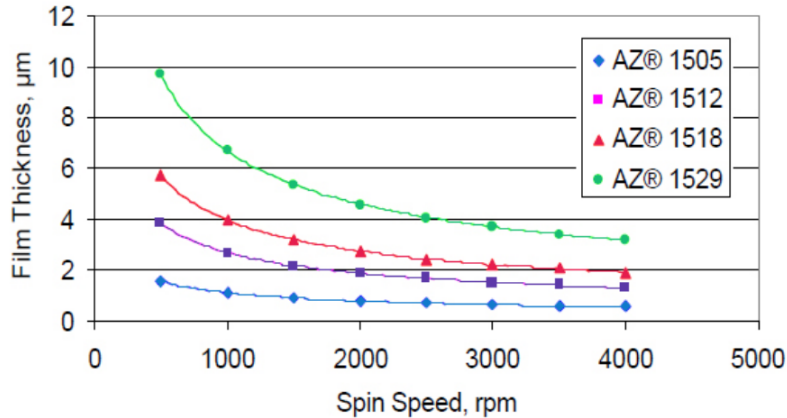


Figure 2.3: Spin curve of AZ-1512HS (Source: EMD Performance Materials^[11])

Issues with HMDS When using HMDS and AZ-1512HS in conjunction, significant amounts of deposition remnants were found on samples as seen in fig. 2.4.

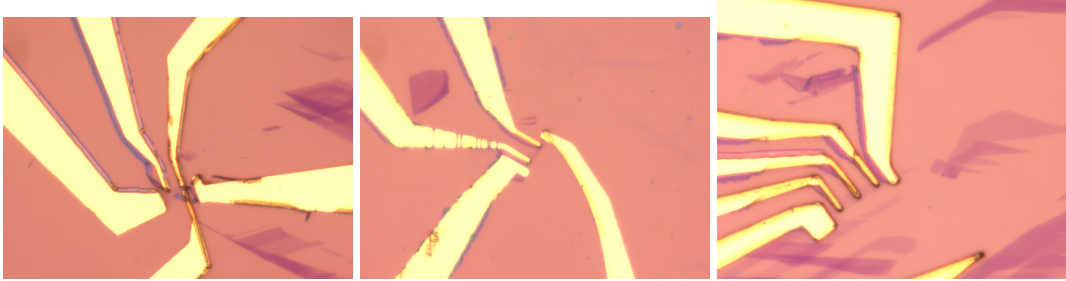


Figure 2.4: Material remnants from lithography. Gold edges exhibit a bluish remnant edge.

This is likely due to metal deposition (i.e. Chromium, see section 2.1.6) forming layers on the sides of lithography wells, as the ‘skins’ have very similar geometry to that of either the wells or the edges. The spinning speeds give resist heights (i.e. the well edge heights) roughly the same as feature width ($\approx 1 \mu\text{m}$ minimum), matching the observed result.

Ultrasonication (see section 2.1.7.1) can be used to attempt to remove edges after lift off, however there is risk of damaging samples of graphene.

LOR-1A & AZ-1512HS The issue with a single layer photoresist processes, outlined above, is that well edges allow deposited materials to adhere, leaving skins. One way to prevent this from happening is to use a multilayer process. Two resist layers are spun onto the sample, with the bottom film being more sensitive to the lithography process than the top (i.e., develops faster, or is more sensitive to exposure). When developed, the bottom layer *undercuts* the top layer. This creates a break between material that is adhered to edges of the well and material that is adhered to the substrate in deposition. This process is depicted in fig. 2.5.

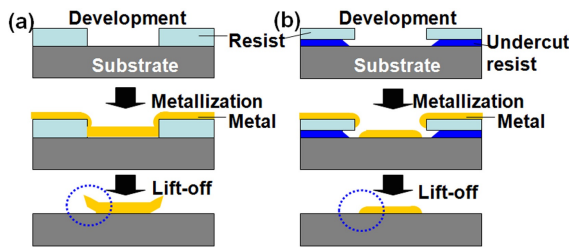


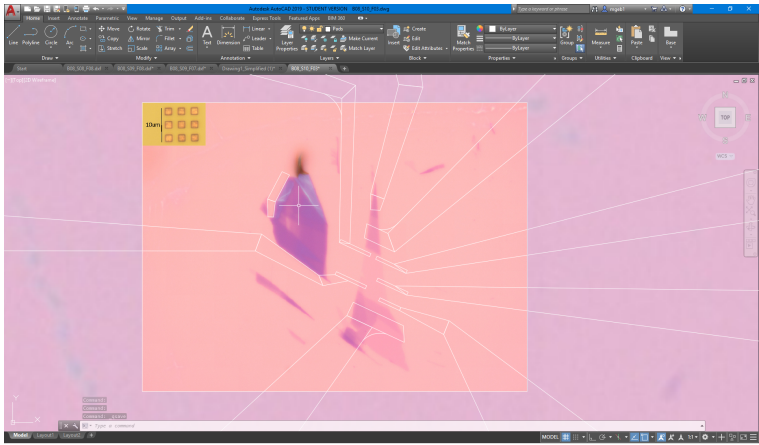
Figure 2.5: Bilayer lithography process (Source: Park *et al*^[12])

LOR-1A is an actinic lift off resist, responding to UV light from 240 nm to 290 nm^[13]. When the resist films are exposed to the developer, LOR-1A is removed below an overhanging AZ1512-HS layer due to additional development, leaving the desired undercut effect.

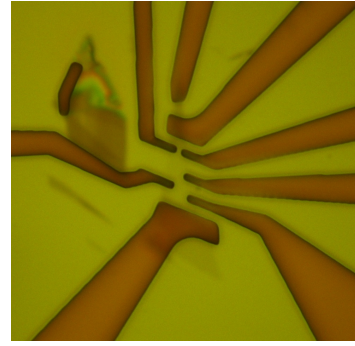
2.1.4.2 Exposure

After spinning, a mask writer tool is used to expose the wafer and resist films to UV light. A mask writer is composed of a mask, or a DMD (digital micro-mirror device) which allows filtering of pixel like squares, based on an input image. Actinic reactions occur from the UV light with the photoresist, forming desired pad structures in the resist. Prepared CAD files are used to generate masks used by the DMD as seen in fig. 2.6.

An important parameter in the mask writing process is the exposure time, which affects the ability to develop fine structures. By using an array of different exposure times (fig. 2.7), the optimal feature result was found for a typical developing time.



(a) DMD masks created using Autocad™. Additional structures are created to help position the mask when using a 20x lens, as graphene can be difficult to see in a mask writer tool.



(b) Photolithography structure from mask writing and development.

Figure 2.6: Photolithography mask writing

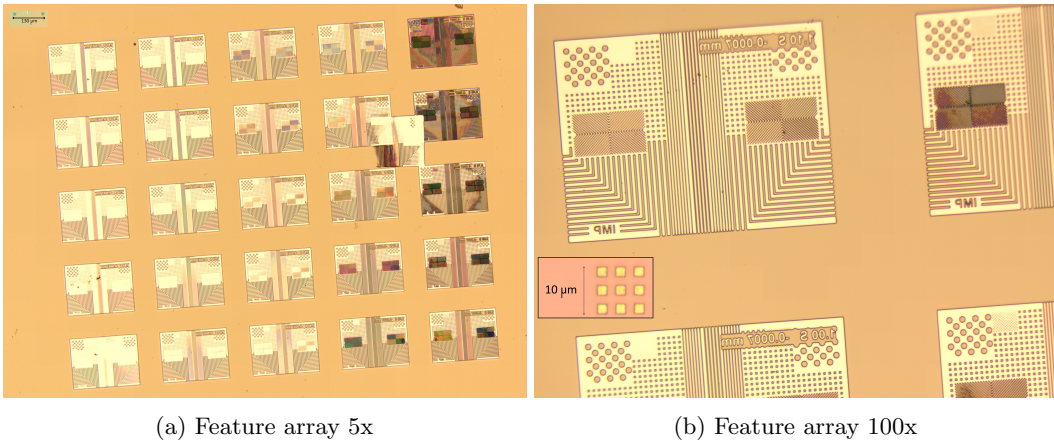


Figure 2.7: Developing an exposure array on SiO_2

2.1.4.3 Developers

Developers are used to dissolve exposed / unexposed areas of photoresist films. We use AZ-726 in conjunction with AZ-1512HS. Using a development time complementary to the exposure time is important to not overdevelop features, as material in proximity to exposed areas is at risk of some structural damage, and developers continue to react with the remaining structure over time.

2.1.4.4 Contact pad dimensions

To make contacts large enough to connect probestation probes to (see section 2.2.2), Au pads were created usually with a minimum dimension of $400\mu\text{m}$ width, and a larger length dimension. This meant that wirebonding was not necessary for small contacts, which saved one step of the measurement process, although PCB boards had been designed with wirebonding in mind (see section 2.1.9).

2.1.5 UV Ozone surface preparation

Large resistances can occur when trying to make contact with graphene. This can be for a variety of reasons. Resist residues between the deposited pads and graphene can be insulating, perhaps non-metallic bonding occurs between deposited metals and graphene, or the oxidisation of metals being deposited (i.e., chromium oxide) could occur.

Several studies by Li *et al.*^[14] and Nath *et al.*^[15;16] have shown the ability to reduce contact resistance of graphene by using UV ozone treatment, to less than $200\ \Omega$, a small contact resistance.

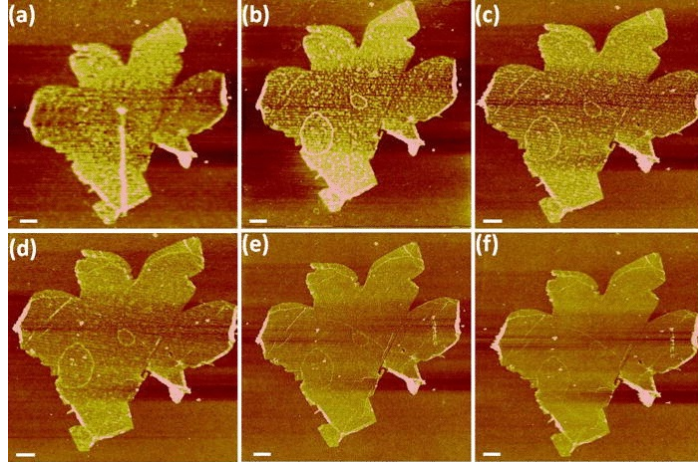


Figure 2.8: Cleaning of graphene using UV Ozone (Source: Li *et al.*^[14])

(a) Before transfer (b) After photolithography (c)→(f) UVO treatment for 5, 10, 16, 22min, respectively. Scale bar: $1\mu\text{m}$.

UV Ozone treatment refers to the use of UV light to generate photochemical reactions on sample surfaces. 185nm light is used to generate ozone O_3 from bonding molecular (O_2) oxygen, while 254nm light is used to dissociate ozone to molecular and singlet oxygen (O_1), the latter of which is reactive with substrate surfaces. Increasing stage temperature also will increase the etching rate that occurs. UV Ozone is used in this context to clean the graphene exposed in our developed wells, as seen in fig. 2.8.

To determine an appropriate etching time for the particular tool used, two wafers with graphene flakes at times of 5m and 15m were cleaned using UV Ozone. The 15m devices were etched away completely, however the 5m device provided the first low resistance contact observed, after many iterations of devices.

2.1.6 Deposition

Once a designed structure is built to make contacts with graphene and cleaned using UV Ozone, material can now be deposited onto the device. There are many different methods, including sputtering and thermal evaporation, however electron beam evaporation (fig. 2.9) was used for these devices, due to its uniformity, control of deposition rate, and the availability of various material crucibles.

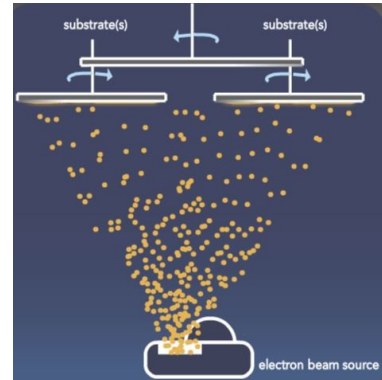


Figure 2.9: E-beam evaporation
(Source:^[17])

Initially 50nm of Au (gold) was deposited with a Cr (chromium) adhesion layer of 5nm to promote contact to SiO_2 . Issues arose with metallic contact to graphene (optically it looked like there should be a connection), and it was suspected that some insulating material was creating a barrier between graphene and the Au metal. UV ozone has already been discussed above as one of the ways to remove unseen polymer, but another possibility was the oxidisation of chromium metal during E-beam evaporation. In case of chromium oxidisation, a thinner layer (2nm) of chromium was instead deposited. This was done intentionally that there might be pinholes due to the thinness of the film, so that there would be some direct contact from gold to graphene, but still the adhesion support from chromium. This deposition amount was introduced the same time as UV Ozone, which marked the success of our first conducting devices.

2.1.6.1 Oxide Protection

In using metal liquids to cover devices with oxides, I found that the gold reacted strongly to the liquid metallic environment, destroying pre-established pads. This is further described in chapter 5, however I was able to overcome this by using additional deposition layers; another layer of Cr 2nm and a layer of SiO_2 20nm. These additional layers do not prevent contact through contact probes and provide insulation from the bulk of metal liquid reactions.

2.1.7 Lift-off

To remove the remaining gold covered photoresist on the substrate, a solvent called PG remover is used to emerge samples at 80 °C. Using a pipette to generate soft fluid flow around the device, the excess gold is slowly removed.

2.1.7.1 Ultrasonication

After lift off, the presence of skin remnants (described in section 2.1.4.1) could sometimes be cleaned off through the use of ultrasonication (fig. 2.12), however this had a large risk of damaging the graphene, seen in fig. 2.13.

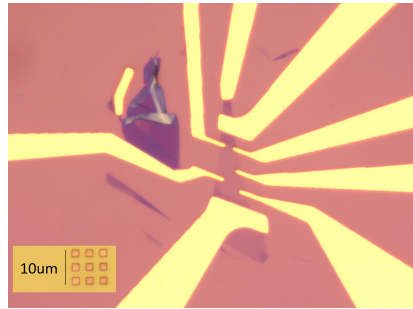


Figure 2.10: Cr/Au/Cr/ SiO_2 contacts. During E-beam evaporation, chromium oxidised, creating an insulating layer to graphene. A thinner layer (2nm) of chromium was instead deposited. This was done intentionally that there might be pinholes due to the thinness of the film, so that there would be some direct contact from gold to graphene, but still the adhesion support from chromium. This deposition amount was introduced the same time as UV Ozone, which marked the success of our first conducting devices.



Figure 2.11: PG Remover liftoff.

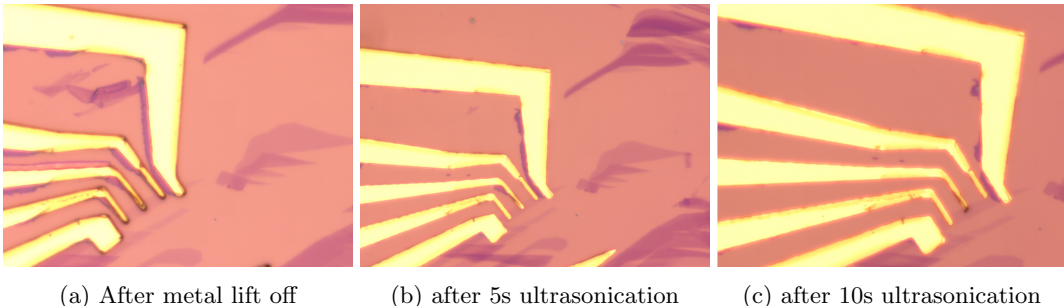


Figure 2.12: Ultrasonication used to remove material remnants from lithography.
Note the movement or loss of gold material on the middle probes.

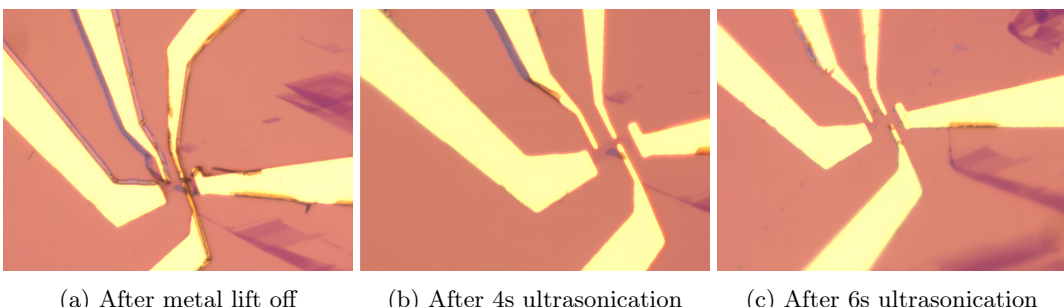


Figure 2.13: Ultrasonication that has broken graphene sample.

2.1.8 Argon/Hydrogen Annealing

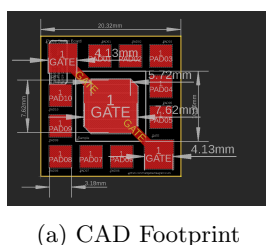
Many researchers who have produced electronic devices from graphene use an argon/hydrogen annealing process to clean their samples from polymer residues remaining from transfer or lithography processes. [18;19;20;21]

We use a process of heating for 30 minutes to 340 °C, annealing with flow rates of 400 sccm Ar / 200 sccm H₂ for 2 hours, before naturally cooling back to ambient temperature.

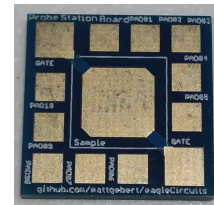
2.1.9 PCB board mounting



Figure 2.14: Ag/H annealing of exfoliated graphene devices



(a) CAD Footprint



(b) Image of product

Figure 2.15: PCB for mounting wafers to connect backgates and wirebond pads of device.

I designed PCB boards for mounting small 1 cm^2 Si— SiO_2 wafers. Wafers are mounted using a conductive silver epoxy (CircuitWorks Conductive Epoxy) from Chemtronics. PCB's were produced through PCBway.com, using a singe layer design with immersion gold surface finishing. Unfortunately the FR4-TG (flame retardant glass transition temperature) was selected at 130-140, which means these boards cannot withstand temperatures above 140°C . PCBway also offer a 180 TG option, which should be used in the future.

These PCB boards provide pads to connect probes to the backgated Si. Additionally, to avoid scratching of lithography pads, extra pads surround the mounting point to wirebond connections to, and then place probes onto.

PCB designs using Autocad Eagle software can be found at github.com/mattgebert/eaglecircuits.

2.1.10 Oxide stamping

Zavabeti *et al*'s^[22] work on thin oxides synthesised by liquid metal introduces two methods to create such oxides. The first involves the exfoliation of oxide layers from the surface of metal droplets, and the second involves the suspension of oxide layers in water, created by injecting gas through the metal liquid. This section will only describe the former exfoliation method in detail, which is used in this project. Refer to chapter 5 for further optimisation and exploration of the liquid metal technique.

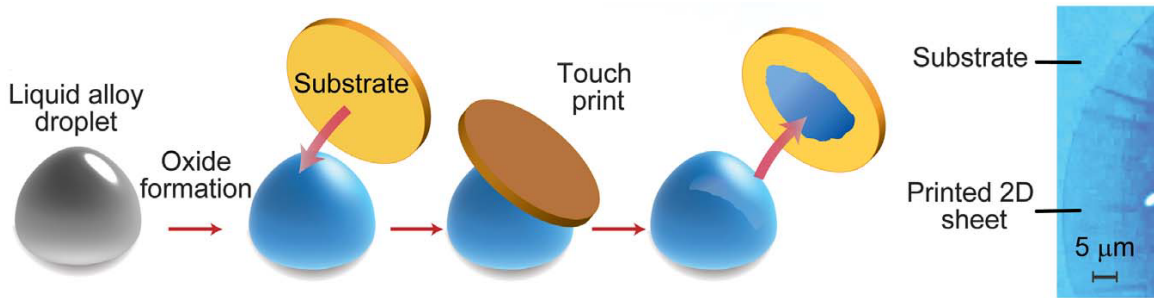


Figure 2.16: Process of liquid metal oxide exfoliation (source: Zavabeti *et al*^[22])

A eutectic gallium melt is made by combining elements such as gallium, indium and tin. At room temperature these alloys are metallic liquids, and form atomically thin oxides on their surfaces. Because the formation of oxides change the Gibbs free energy of the system, those that provide the greatest reduction dominate the surface^[22]. After the melt is formed and exposed to oxygen for some time, the oxide is isolated by a van der Waals exfoliation technique, touching the liquid metal droplet to the solid substrate, as seen in fig. 2.16.

For the synthesis of AlO_3 , aluminium pieces are cleaned using a tissue and acetone, before being cut up into a few mm long segments. After heating a gallium based melt into a liquid inside a glovebox with roughly 0.2-0.3% oxygen, the gallium and aluminium are ground together using a porcelain mortar and pestle. The aluminium makes up about 2% of the total weight. After this, some time is taken for the oxide to form on the surface of the liquid metal (put on glass slides for accessibility. Glass slides are cleaned with water/ultrasonic bath). Substrates are touched lightly, and should be able to be removed from the liquid metal droplet without adhering the liquid, but obtaining a thin oxide layer.

2.2 Measurement techniques

To measure the electrical properties of graphene devices (such as those detailed in section 2.1), particular equipment and methods are employed to observe relevant properties.

2.2.1 Four probe measurements

Four probe measurements, also known as Kelvin sensing, utilise four probes to make a more accurate measurement than regular two probe measurements.

Conventional multimeters use a probing voltage with a galvanometer to detect a current running through a sample (in this case, graphene). Based off the detected current, a measurement can be made of the resistance for the known voltage. Because exfoliated graphene can have very small channel widths, it is very sensitive to large currents and consequently makes using a multimeter dangerous. Using a multimeter would be fine however, for large area CVD graphene.

One advantage of using a 4 probe measurement is that you can use a current-limiting resistance. Placing a resistance in series with your devices allows the creation of a nearly constant-current source from an applied voltage. The choice of resistance is such much larger that the sample ($> 100\times$) to ensure the current is well approximated by the voltage across the sample and resistance ($V_{sc} - V_{GND}$) divided by the limiting resistance (an approximation to a voltage divider eq. (2.1)).

$$I_{sc} = \frac{V_{sc} - V_{GND}}{R_{lim} + R_{sample}} \approx \frac{V_{sc} - V_{GND}}{R_{lim}} \quad \forall \quad R_{lim} \gg R_{sample} \quad (2.1)$$

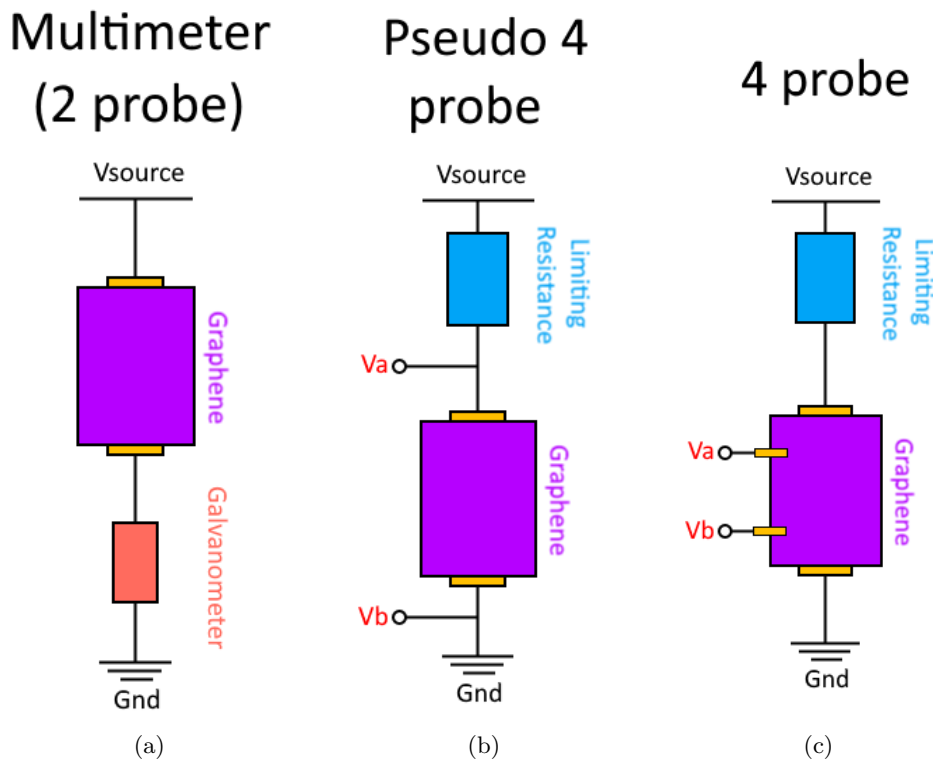


Figure 2.17: Schematics of resistance measurements. (a) A multimeter provides little control over the current through the sample, and measures any resistance formed between the gold contacts and the graphene. (b) A pseudo four probe measurement uses a voltage difference across the device to calculate its resistance, inclusive of the series resistance due to the gold contacts. (c) A four probe

measurement uses a voltage difference measured by probes at different points on the sample material, thereby avoiding any contact resistance included in series, and sampling the voltage along the sample.

This allows control of the current running through your sample, ensuring safe limits, and means the resistance of your sample will affect the current flow to less than 1%. By observing the voltage difference across the sample, a resistance can be inferred from the flowing current. Typical exfoliated graphene devices used in this project have a measured resistance on the order of $\approx 5 \text{ k}\Omega$ (eq. (2.2)).

However, the most significant advantage of using a 4 probe measurement is the ability to avoid including contact resistance, created by the junctions between contact pads and the material of interest (graphene). This is illustrated in fig. 2.17. A 4 probe measurement uses a voltage difference measured by probes at different points on the sample material, thereby avoiding any contact resistance included in series, and sampling the voltage along the sample. An example resistance calculation is shown in eq. (2.2).

$$R = \frac{V_{b-a}}{I_{sc}} \approx \frac{V_{b-a}}{(V_{sc} - V_{GND}) / R_{\text{limit}}} = \frac{5 \times 10^{-3} \text{ V}}{1 \text{ V}/10^6 \Omega} = 5 \text{ k}\Omega \quad (2.2)$$

2.2.1.1 Sourcemeters

A sourcemeter has the ability to source and measure a stable DC voltage or current. They provide precision, low noise and stability. Dr. Battacharyya and I used Keithley 2400 SourceMeters^[23] which source voltage from $5\mu\text{V}$ to 210V, and current from 50pA to 1.05A, and can deliver 520 readings per second at $5\frac{1}{2}$ digits (ie, 199999).

A source meter is used in 4 probe measurements to apply a constant, controllable gate voltage to the Si as directed in fig. 2.18, whilst being able to limit the current flow. Changing the potential of Si under SiO_2 changes the charged carrier density (electrons, holes) on graphene by using the SiO_2 as a capacitor dielectric. This allows the measurement of the resistivity of graphene as a function of carrier density.

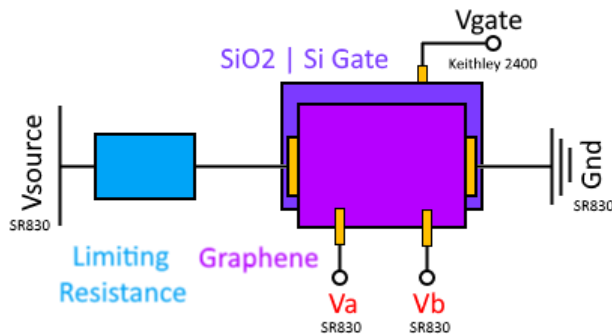


Figure 2.18: Instrumentation connections to a gated graphene FET, using a Keithley 2400 SourceMeter and a SR830 Lock-In Amplifier.

2.2.1.2 Lock-in amplifiers

A lock in amplifier is used to measure very small AC signals. This project used a Stanford Research 830 Lock-in amplifier^[24], which uses a significant amount of digital signal processing (DSP) for its functionality. It operates on the principles of signal mixing - multiplying an input signal (f_s) that is expected at a particular frequency by a reference signal (f_r). This mixing generates a DC signal whose amplitude can be measured, directly inferring a signal strength. An example calculation of mixing is shown below in eq. (2.4).

$$f_s \otimes f_r = \cos(\omega_s t + \phi) \otimes \cos(\omega_r t) \quad (2.3)$$

$$\begin{aligned}
&= [\cos(\omega_s t) \cos(\phi) - \sin(\omega_s t) \sin(\phi)] \otimes \cos(\omega_r t) \\
&= \cos(\phi) \frac{1}{2} [\cos((\omega_s + \omega_r)t) + \cos((\omega_s - i\omega_r)t)] \\
&\quad - \sin(\phi) \frac{1}{2} [\sin((\omega_s + \omega_r)t) + \sin((\omega_s - \omega_r)t)]
\end{aligned} \tag{2.4}$$

When the two frequencies ω_s and ω_r are close, then the sinusoidal components $\omega_s - \omega_r$ form a DC component, while high frequency components can be filtered. Only noise that is close to the signal frequency will be picked up in the filtering, with the consequence of low frequency AC output. This is advantageous, as many electronic noise sources follow a 1/f (or pink/flicker) noise spectrum [25;26], meaning that we can avoid high amplitude, low frequency noise.

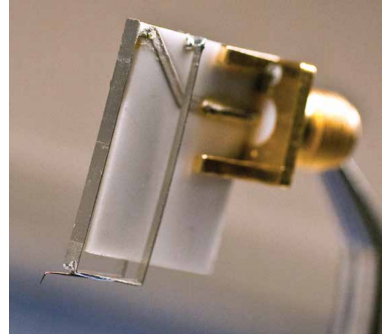
The lock in amplifier uses a phase locked loop to generate a reference signal, which is a particular control circuit. The lock in amplifier can either run independently, generating its own consistent phase locked output, or can be locked to an external signal. We use the former in our measurements, to cast a slow 17Hz signal of nearly constant amplitude 1V_{rms} across my graphene devices and the limiting resistor, providing a nearly constant amplitude AC current.

A voltage difference is calculated between probes on graphene by the lock in amplifier and outputted. The real component of the voltage difference and the complex phase are recorded - we expect the bulk transport in graphene to be resistive (ie the output is in phase with the input), and a phase is measured to confirm that as we measure.

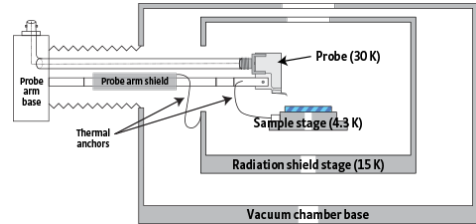
2.2.2 Probe station



(a) LakeShore probestation, with coolant inlet, 6 probe arms, vacuum seal and microscope camera.



(b) Tungsten spring probes, 25 μm radius tip



(c) Schematic diagram of probestation, showing connections from probe arms to sample stage and temperature limits of elements

Figure 2.19: LakeShore probestation

A LakeShore cryogenic probestation (fig. 2.19) was used to load sample wafers and measure their electronic properties under controlled conditions. In particular, we will touch on temperature control, vacuum ability, and the risk of static discharge.

2.2.2.1 Vacuum

A roughing pump is used in conjunction with a turbo pump to create pressures of 1.5×10^{-2} mBar and 5×10^{-5} mBar (turbo at 1.35 kHz operational frequency). This pumping removes any trapped oxygen and contamination of gasses that might condense onto our sample of graphene at low temperature.

2.2.2.2 Temperature control

Temperature is controlled by a combination of heating and cooling power. The metallic inlet protruding from under the main stage in fig. 2.19 allows the flow of liquid nitrogen/helium through the sample stage to cool down the sample. This process is illustrated in fig. 2.20.

Heating is provided via a 50W calibrated silicon diode. Thermocouples with high accuracy allow the ability to control the heating power to stabilise to a setpoint temperature, with small fluctuation. This is achieved by the use of a PID controller system, where the measured temperature difference from a setpoint is used to control the diode power. By using the proportional, integral and differential gains, rapid and stable responses to shifts in desired temperature are be controlled.

- Proportional gain adds some power based on the difference from the desired solution.
- Integral gain ramps the power over time, based off long term difference. This prevents offsets from a final setpoint.
- Differential gain only considers the changing response. It smoothens trajectory of PI controller, reducing overshoot and stabilising levels faster.

2.2.2.3 Static Discharge

Care needs to be taken when using the probestation with small graphene samples. Static discharge can cause large potential differences across graphene, consequently burning the sample by a high current. Discharge can be protected against by taking some precautions below.

BNC cables employ a coaxial (ground and signal) wire configuration, and are used to connect to the probestation. This ensures the probestation shield is grounded, the same as the instrument ground. This protects the device from any external static buildup. If the probes are then grounded, they are at the same potential as the shield.

Additionally, when a measurement was not taking place, BNC connections to the device were grounded using 50Ω terminators, connected via T terminals to avoid floating connections and minimising static while connecting terminators. This meant that any external charge would have a low resistance current path to flow, thereby protecting the sample.

Static straps were also worn and connected to the instrument ground to ensure no clothing item would build up static on an individual.

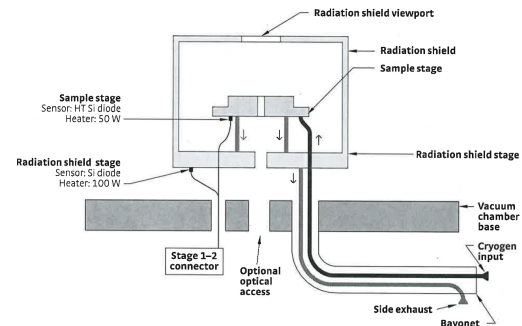


Figure 2.20: Probestation refrigerator
Figure 2.20 shows a schematic diagram of a probestation refrigerator. The diagram illustrates a multi-stage cooling system. At the top, a 'Radiation shield viewport' is shown above the 'Radiation shield'. Below the shield is the 'Sample stage', which contains a 'Sensor: HT Si diode' and a 'Heater: 50 W'. To the left of the sample stage is the 'Radiation shield stage', which also contains a 'Sensor: Si diode' and a 'Heater: 100 W'. A 'Stage 1-2 connector' is located between these two stages. An 'Optional optical access' port is shown on the left side. The central part of the diagram shows the 'Vacuum chamber base' with a 'Cryogen input' and a 'Side exhaust Bayonet'. Arrows indicate the flow of liquid nitrogen/helium through the stages and into the base.

2.2.2.4 Probes

A combination of regular and flexible tungsten probes are used in the probestation to make electrical connections to samples. When touching probes down, the respective BNC was connected to a $10\text{ M}\Omega$ resistance terminator. Rather than protecting from external static, this was in case the sample (sometimes doped) was resting at a potential other than ground, and had free charge to discharge. A high resistance terminator reduces this resulting current and increases the time to drain the same amount of charge, before allowing the connection of an appropriate ground.

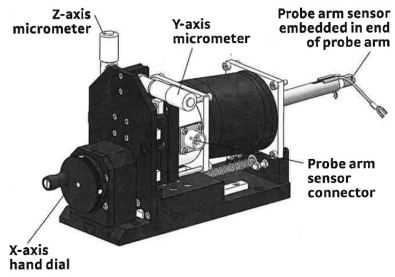


Figure 2.21: Probestation micro-manipulated stages

Chapter 3

Characterisation of graphene

3.1 Raman spectroscopy

Raman spectroscopy uses monochromatic light to observe scattering processes on an incident material. Four fundamental processes describe the scattering behaviour: IR absorption, Rayleigh scattering, or (anti) Stokes Raman scattering. The latter (two) processes scatter light, by interactions with phonons or other excitations. This changes the incident light's momentum and energy, resulting in a frequency shift. By measuring the returning light and its spectral distribution, information is gained of the vibrational modes within the material. Devices such as charged coupled devices (using MOS or CMOS transistors) allow for sensitive measurements of the light across different frequencies. Photons that are scattered with the same initial energy (Rayleigh Scattering) are filtered.

3.1.1 Raman in graphite

Historically, the Raman profile for graphite is well established^[27]. Since the invention of the laser to make sensitive, monochromatic measurements, Raman spectroscopy conducted in the 1970's had yielded a distinct profile of the phonons existing within graphite^[28;29;30]. At the beginning of the 80's Vidano's group profiled graphite samples across multiple Raman wavelengths, properly profiling different peaks^[27].

Peaks are listed as follows:

- **G** ($\approx 1580/\text{cm}$) The active $2E_{2g}$ mode of the hexagonal symmetry group. This traditionally has the highest peak intensity in graphite, and is doubly degenerate.
- **2D** ($\approx 2700/\text{cm}$) Higher order scattering, and overtone of D. Second highest peak in graphite. Relabelled as the 2D peak by Ferrari, originally written as G' peak.
- **D** ($\approx 1360/\text{cm}$) Attributed to edge modes (ie zone boundaries) that appear from relaxed wavevector selection rules.
- **D'** ($\approx 1620/\text{cm}$) Splitting from degenerate E_{2g} due to disorder.
- **D''** ($\approx 2950/\text{cm}$) Higher order scattering.

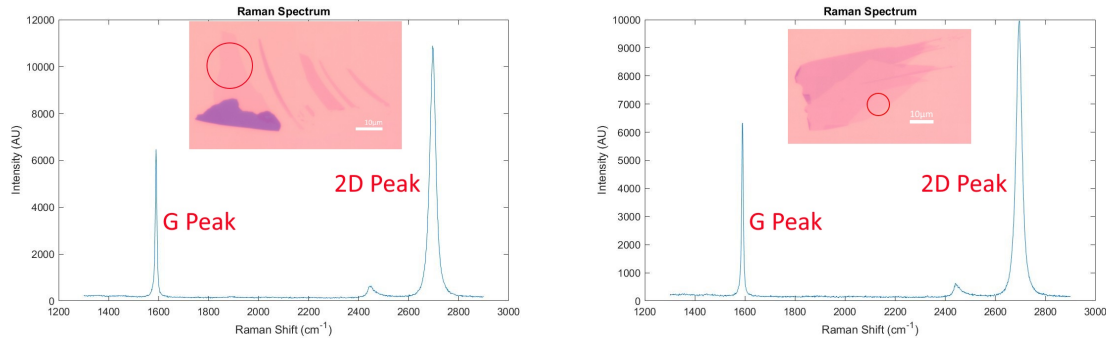
In graphite, the G peak is normally dominant and the 2D peak is split into at least two components at 1/2 and 1/4 amplitudes of the G peak.

3.1.2 Raman in graphene

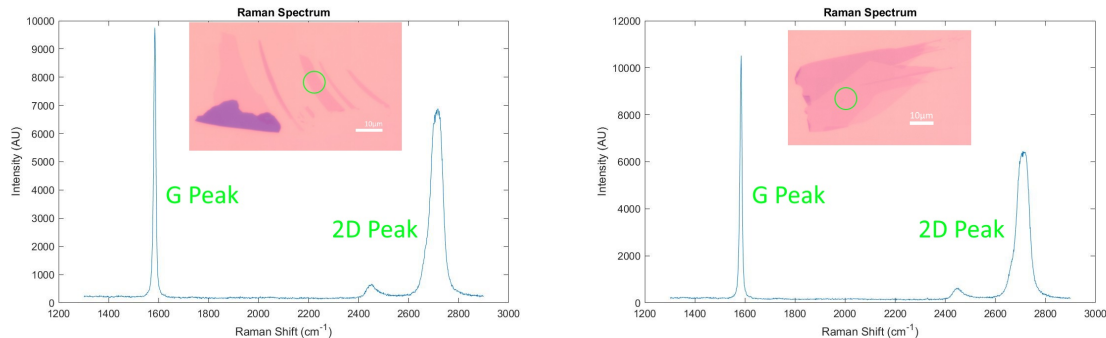
Differing layer numbers of graphene produce unique Raman signals^[31;32]. This variance in the amplitude and central frequency of maxima. The signals are unique because the vibrational and electronic properties of monolayer, bilayer and multilayer are distinct. Ferrari *et al.* observed that Raman is a useful tool for distinguishing between these layers.

Two particular characteristics are useful for characterising layers. Firstly the amplitude of the 2D peak is roughly on the order of 2x that of the G peak in graphene. This ratio drops as the number of layers increases. Only the single layer and bilayer peaks are easily distinct from higher numbers of layers, which are somewhat indistinguishable.

This characteristic is clear in the data acquired of numerous graphene samples shown below in fig. 3.1.



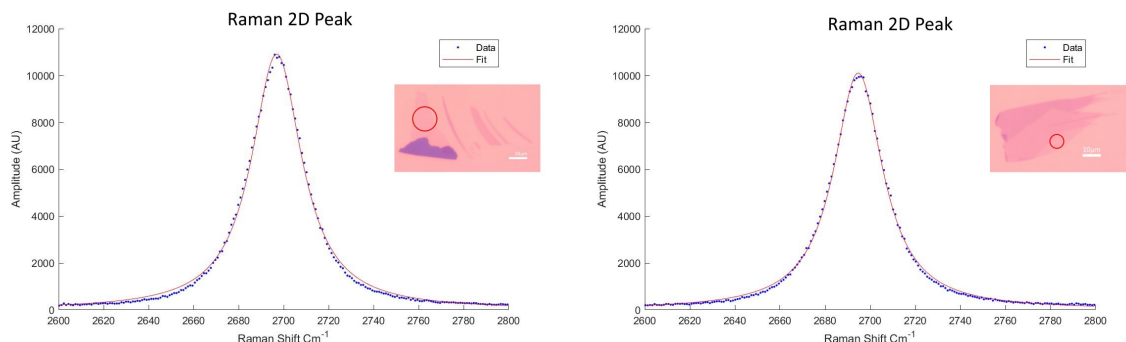
(a) Graphene Raman spectrum. The 2D peak is roughly 2x the amplitude of the G peak.



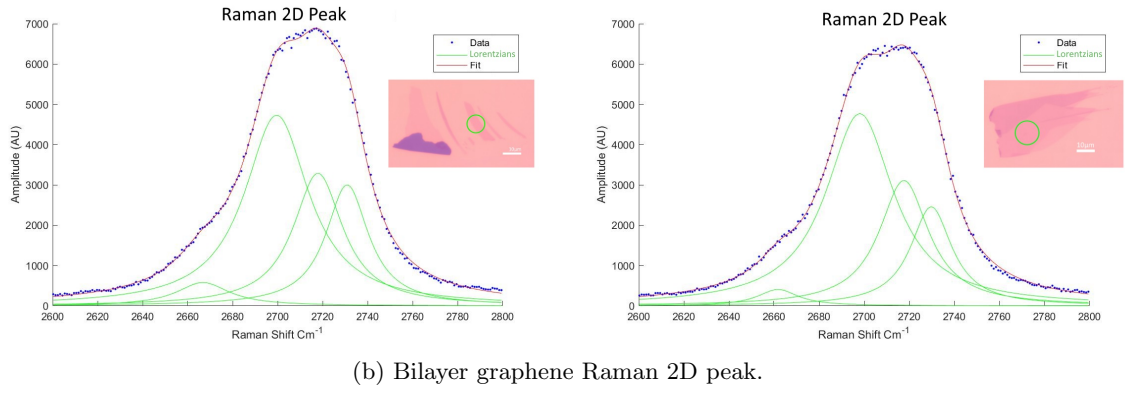
(b) Bilayer graphene Raman spectrum. Broader 2D peak that is $\approx \frac{3}{4}$ of the amplitude of the G peak.

Figure 3.1: Ratio of G to 2D Peaks in various levels of graphene

Secondly, the 2D peak slowly shifts right and broadens as layers increase. This is distinguishable between a single layer, two layers and multiple layers. For a single layer, the peak fits very well to a single resonance lorentzian. For two layers, 4 lorentz peaks are used to fit the broader 2D resonance.



(a) Graphene Raman 2D peak.



(b) Bilayer graphene Raman 2D peak.

Figure 3.2: Raman 2D fitting of graphene and bilayer

The theoretical picture is quite intuitive for the broadening of the 2D peak seen in fig. 3.2. Because the 2D peak relates to disorder, and not directly a mode of geometric structure of graphene, the 2D peak is coupled to the electronic structure of graphene (see fig. 3.3). A single layer of graphene has two bands that meet at dirac points (see section 1.3.1.2), which allows singular transitions in the momentum/energy profile. A bilayer of graphene has two extra non-degenerate bands instead, allowing a possibility of 4 slightly different transitions near the same energy/momentun profile, contributing to the broadness seen in the Raman spectrum.

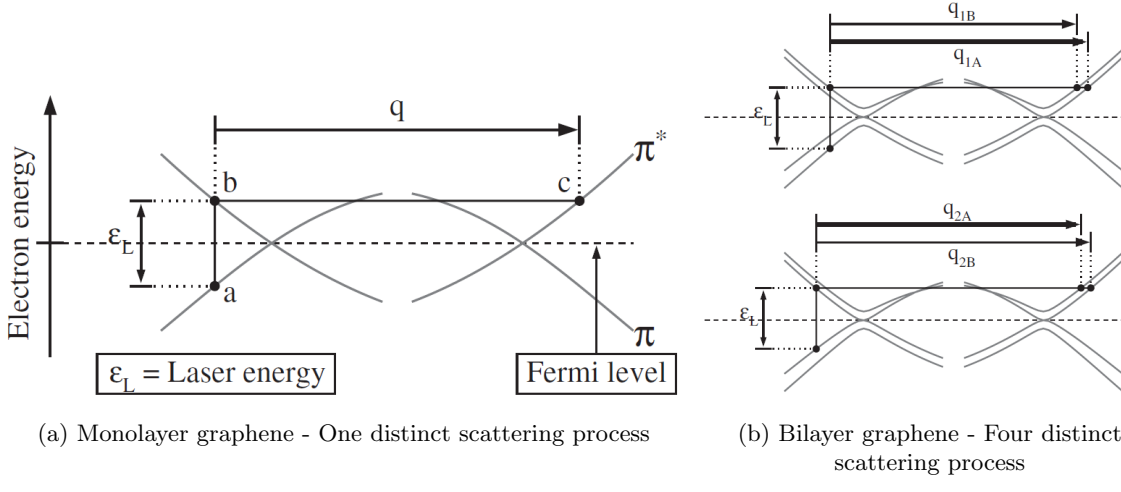


Figure 3.3: Raman scattering processes in graphene and bilayer graphene, coupled to the electronic structure. Each transition results in a unique change of momentum and energy.

(Source: Ferrari *et al.*^[31])

3.2 Optical microscopy

Under a microscope graphene can be optically observed on particular substrates. Blake *et al.* has studied the optimal wavelengths in which to observe graphene, based on the oxide thickness (SiO_2)^[33]. We use 285 nm SiO_2 on top of Si to make graphene most pronounced in green wavelengths, which is also the most sensitive colour to the human eye (see fig. 3.4). A consequence of this strong contrast is that monolayer graphene can be optically identified without the need for more other measurements such as Raman or atomic force microscopy^[34;35].

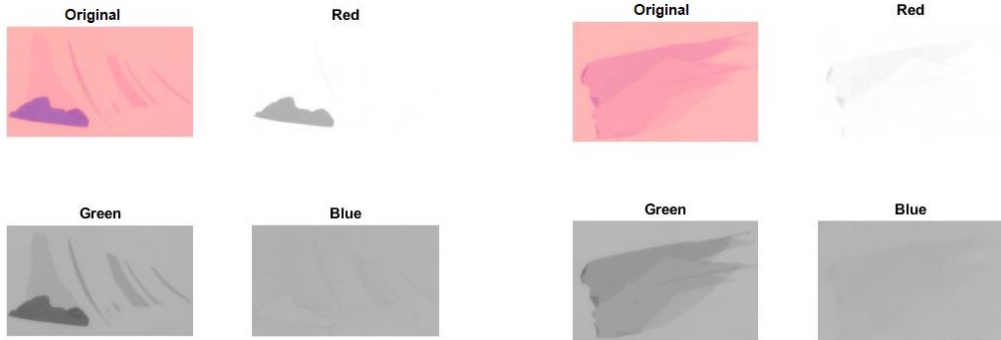


Figure 3.4: RGB decomposition of optical images of graphene on 285nm SiO₂. Most contrast for single or few layers of graphene comes from the green component as desired.

3.2.1 Contrast imaging

Graphene absorbs 2.3%, passing $\approx 97.7\%$, of the light incident on it. This opacity is actually defined by the fine structure constant, physically determined by fundamental quantities^[36]. The fine structure constant describes the fundamental electromagnetic interaction strength of particles. This opacity is one of the few phenomena in condensed matter physics that doesn't depend on material parameters, and is pretty spectacular (excuse the optical pun) to consider.

Graphene exhibits a universal electrical conductance minimum of $\approx 4(e^2/h)$ (see section 1.3.1.3), and as a result^[37] the optical conductance is also expected to have a fundamental value, behaving independent of frequency (to a broad range of photon energies). This uniform frequency response is due to the linearity of the electronic band structure around the dirac points, which phonons interact with.

$$\alpha = \frac{\pi e^2}{\hbar c} \approx \frac{1}{137} \quad (3.1)$$

$$\pi\alpha \approx 2.3\% \quad (3.2)$$

We can use this property of graphene's optical transmittance to perform contrast imaging of graphene, identifying single layers from the contrast between the substrate beneath and the flake of interest.^[34;35;38]

If light passes from a source through the graphene, reflecting from the SiO₂ and passing back through the graphene, then we expect approximately 5% absorbtion of our incident intensity, which will cause a contrast change. We calculate a contrast value for each pixel by using the green pixel value of each square ($G \in [0, 1]$) and taking the difference from the background mode G_0 .^[38;35] Dividing by the background mode gives a percentage change.

$$C = \frac{G - G_0}{G_0} \quad (3.3)$$

This contrast formula takes a green colourvalue representing the background contrast, and observes the percentage change when layers of graphene are on top of it. This percentage absorbtion should roughly match the expected 2.33% per transmission through graphene, as the pixel value approaches black (value $G = 0$) with more layers.

Figure 3.5 and fig. 3.6 both clearly indicate peaks for single layers near 6% contrast, and multiples of that for larger layers. This is a little higher than expected, but given RGB capture is 0-255, the uncertainty in pixel capture is roughly $1/255 \approx 0.4\%$ making this deviation reasonable.

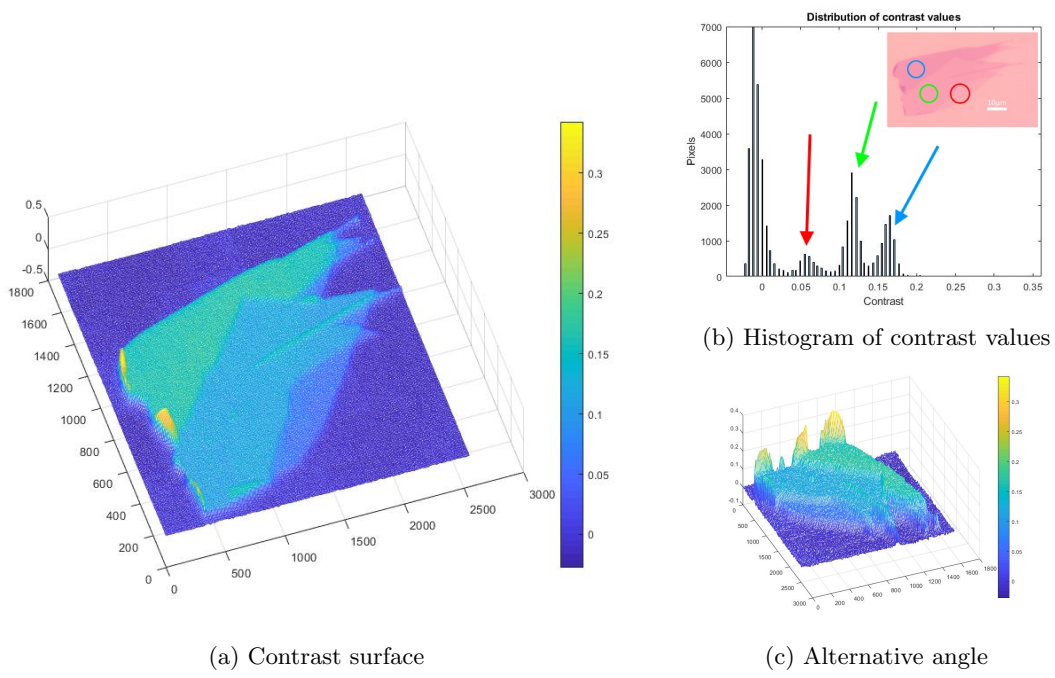


Figure 3.5: Contrast imaging of sample 1.

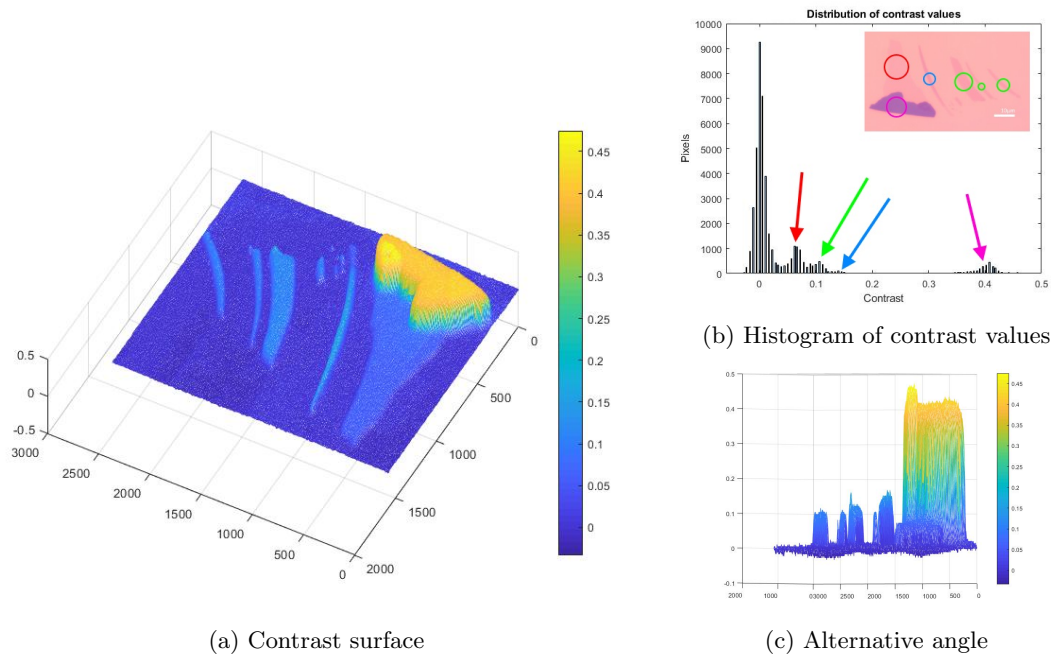


Figure 3.6: Contrast imaging of sample 2.

Chapter 4

Electrical measurements of pristine graphene

Graphene devices first need to have their transport properties measured in their pristine condition, prior to the application of thin oxides. Doing this will allow a comparison of the electrical transport properties before and after transfer, to see if there's any resulting enhancement. Here I analyse the resistance measurements taken for both graphene and CVD graphene. I will consider their dependence upon gate voltage and temperature.

4.1 Resistance to resistivity

The resistivity of a material is a core property describes its behaviour in a bulk geometry. For 3D materials, resistivity is in the units of Ohms per meter. You can think about this single length proportionality coming from flowing charge through a cross section, but over some length. In 2D materials, resistivity is measured in Ohms, because there are only two dimensions, the length and the width of flat material. The partial form of the resistivity is listed in eq. (4.1), where $w(L)$ is the width of the material as a function of Length.

$$\partial R = \frac{\rho}{w(L)} \partial L \quad (4.1)$$

In most cases of devices we make, the geometry between probes can be described by either a rectangle or a trapezoid. There will be a resulting geometric factor that converts our resistance to resistivity.

$$\rho = \mathcal{G} \times R \quad (4.2)$$

For a rectangle, the width is independent of the length, and the geometric factor to convert resistance to resistivity becomes:

$$\mathcal{G} = \frac{w}{L} \quad (4.3)$$

For a trapezoid, such as in the width is linearly dependent upon length, and the geometric factor can be found as follows:

$$w(x) = w_0 + \frac{x}{L}(w_1 - w_0) \quad (4.4)$$

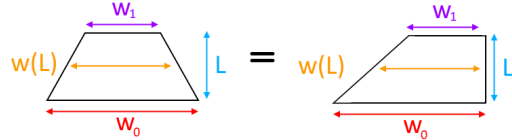


Figure 4.1: Two equivalent geometries of trapezoids.

$$\frac{1}{\mathcal{G}} = \int_0^L \frac{1}{w(x)} dx = \frac{l(\log[lw_0] - \log[lw_1])}{w_0 - w_1} = \frac{l \log[w_0/w_1]}{w_0 - w_1} \quad (4.5)$$

$$\Rightarrow \mathcal{G} = \frac{w_0 - w_1}{l \log[w_0/w_1]} \quad (4.6)$$

In the limit $w_1 \rightarrow w_2$, this result is consistent and returns to the rectangular case. I have included a few samples of which the geometric factor has been calculated:

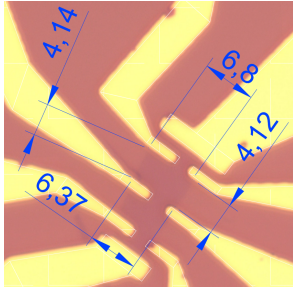


Figure 4.2: Geometry of exfoliated device 6 (EXF06). Units are in μm .



Figure 4.3: Geometry of exfoliated device 4 (EXF04). Units are in μm .

This quantity is unclear for the transferred CVD graphene on top of gold pads because of the wide coverage across gold and short distances between current pads and voltage pads, however the relevant geometric quantity can still be found through the gate voltage dependent resistivity (Refer to section 4.2.1).

4.2 Gate dependent conductivity

After converting resistance measured to resistivity, I invert the resistivity to conductance. This now allows the fitting the gate voltage dependent conductivity (eq. (4.7)).

$$\sigma = \sqrt{(N^* e \mu)^2 + \left(\rho_S + \frac{1}{N e \mu} \right)^{-2}} \quad (4.7)$$

Here N^* (also written as \mathcal{N}) is the ‘residual carrier density’ (m^{-2})^[39], N is the carrier density (m^{-2}), e is the elementary charge, μ is the mobility (m^2/Vs) and ρ_S is a resistivity parameter that affects the curvature of the gate voltage dependent conductivity, particularly in the high voltage limits, but its origins are unclear. The carrier density N is calculated by considering the accumulated charge

at the gate. This amount can be calculated for each device, by considering the capacitance of 285nm SiO₂ and the difference in gate voltage from the Dirac point.

$$N(V_G) = \frac{C_g}{e} |V_{\text{Dirac}} - V_G| \quad (4.8)$$

$$C_g = \epsilon \frac{A}{d} = 3.8 \times 8.85 \times 10^{-12} \frac{1}{285 \times 10^{-9}} \approx 1.2 \times 10^{-4} \quad (4.9)$$

In using this fitting function, I only apply the fit to one side of the V_g vs ρ curve's data at a time. This means that the mobility parameter μ is treated separately for hole and electron like conduction.

Fitting was performed on conductivity data, so that parameter fits were sensitive to curvature far from the Dirac point. Unfortunately, this also meant that sensitivity to the Dirac point was lacking during fitting. As a result, I added extra weighting to data near the Dirac point, to ensure the charge impurity parameter \mathcal{N} enforced a good match at the minimum conductivity turning point. This action I took is justified, because if the impurity parameter is not properly fitted, then linked parameters such as the mobility will be incorrectly determined. An example fit for EXF06 is shown in fig. 4.4, the same parameters plotted over resistivity and conductivity:

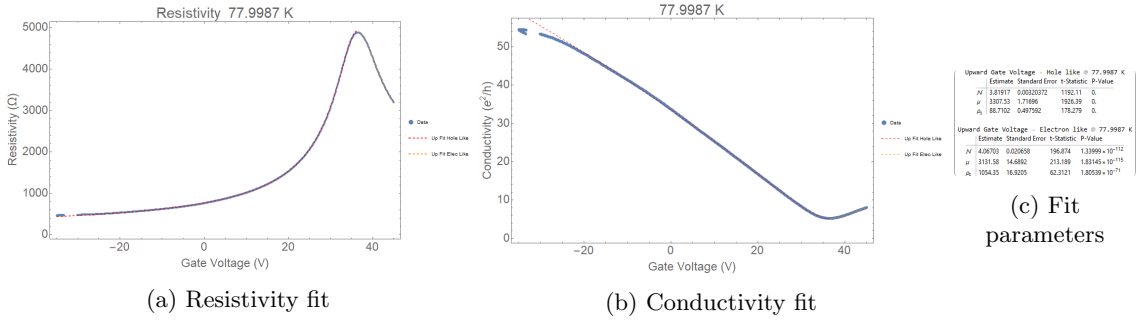


Figure 4.4: Gate dependent transport of EXF06 at 78K.

Note parameter units are: mobility μ in cm²/Vs, \mathcal{N} in $\times 10^{15}/\text{m}^2$, and ρ_S in Ω

Here the conductivity has been scaled in terms of the conductivity quantum, e^2/h . Further fits for devices at different temperatures can be found in appendix A.

4.2.1 Finding the geometric factor of CVD graphene

I previously mentioned the issue with finding a geometric factor for CVD graphene. It turns out that from finding the residual carrier density parameter \mathcal{N} , we can scale our data to match the correct theoretical mobility μ predicted for that particular \mathcal{N} . The theoretical data we use to find the matching mobility is provided in appendix B.

A new fit doesn't change the determined \mathcal{N} value, because the mobility μ is a parameter that scales the minimum conductivity point along with the conal regions $\rightarrow \mathcal{N}$ is independent of scaling.

My method of determining the geometric value is as follows:

1. Find minimum conductivity value
2. Scale conductivity data such that minimum conductivity is $\approx 4 (e^2/h)$. This is a ballpark figure for most graphene samples^[40], and will allow us to get close to the desired mobility μ and residual carrier density \mathcal{N} .
3. Fit the conductivity data to eq. (4.7) to find \mathcal{N} and ρ_S .
4. Refer to the theoretical data in appendix B to find the corresponding mobility μ_0 for the particular \mathcal{N} .

5. Scale conductivity by λ such that $\sigma|_{\mathcal{N}, \rho_s, \mu \rightarrow \mu_0} \times \lambda = 4e^2/h$
6. Repeat step 3 to make sure μ and \mathcal{N} match up.
7. Calculate geometric factor $\frac{1}{G} = \frac{\text{Scaled minimum conductivity}}{\text{Original minimum conductivity}}$

To check the validity of this method, I compare the geometric factors calculated above for EXF06 to the numerically determined values.

EXF06 Raw data minimum conductivity was originally $8.5061 (e^2/h)$ at 88K. All conductivity values were divided by 2.1265 to bring the minimum back to 4. Fitting was then done to find the residual carrier density \mathcal{N} , seen in fig. 4.5.

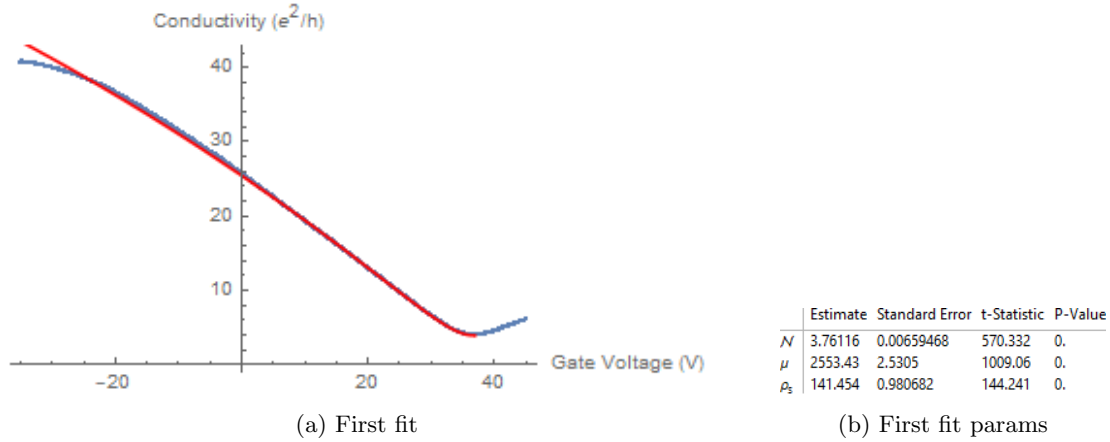


Figure 4.5: First fit to find \mathcal{N}

Finding the value $N^* = 3.76 \times 10^{15}$ in appendix B, we interpolate the corresponding mobility to $0.3460 \text{ m}^2/\text{Vs}$. Then finding the scaling factor for the conductivity:

$$\lambda \times \sigma [\rho_s \rightarrow 141, \mu \rightarrow 0.3460, \mathcal{N} \rightarrow 3.76 \times 10^{15}] = 4 \quad (4.10)$$

$$\implies \lambda = 0.743448 \quad (4.11)$$

The conductivity is then scaled by the reciprocal of this value, so that the minimum conductivity moves from 4, and allows the appropriate scaling of μ to match \mathcal{N} . The minimum conductivity is now scaled to $5.38034 (e^2/h)$.

Performing a second fit to check the new value,

	Estimate	Standard Error	t-Statistic	P-Value
\mathcal{N}	3.79866	0.00321997	1179.72	0.
μ	3409.61	1.80441	1889.59	0.
ρ_s	97.5059	0.500944	194.644	0.

Table 4.1: Second fit to confirm μ scaling

The mobility is now $3409.61 \text{ cm}^2/\text{Vs}$ which is very close to $3448.28 \text{ cm}^2/\text{Vs}$ (the tabled value corresponding to $\mathcal{N} = 3.79353 \times 10^{15}/\text{m}^2$). I could perform a few more iterations to get the mobility even more closer to the theoretical, but seeming I am interpolating non-linear data between rows, I deemed this to be unnecessary, particularly given the final result.

Now finding the relative factor between the original minimum conductivity and the scaled minimum conductivity:

$$\frac{1}{\mathcal{G}} = \frac{5.38034}{8.5061} = 0.632524 \quad (4.12)$$

$$\implies \mathcal{G} = 1.58097 \quad (4.13)$$

This is almost exactly a 1% difference from our image found geometric value of $\mathcal{G} = 1.59773$, which shows the reliability of this method. Its noteworthy that finding the geometric value from images will have a degree of uncertainty ($\approx 10\%$) in the width and length values used, due to the scaling of images and placement of dimension markers.

CVD01 Performing the same analysis in our dataset for CVD graphene, I find the minimum conductivity scales from $47.7959 (e^2/h)$ to $4.3794 (e^2/h)$, when the mobility μ and residual carrier density \mathcal{N} converge on $0.157402 \text{ m}^2/\text{Vs}$ and $6.67275 \times 10^{15}/\text{m}^2$ respectively (rows 63 & 64 of appendix B). This results in a geometric factor of $\mathcal{G}10.7959$.

Considering the visual geometry of our CVD graphene in fig. 4.6, this is likely a reasonable geometric factor, given for a rectangular case \mathcal{G} goes as W/L . In the figure, the majority of the current probably flows through the gold probes rather than through the bulk graphene, and considering the width to length ratio between those probes, I'd suggest its approximately a factor of 10.

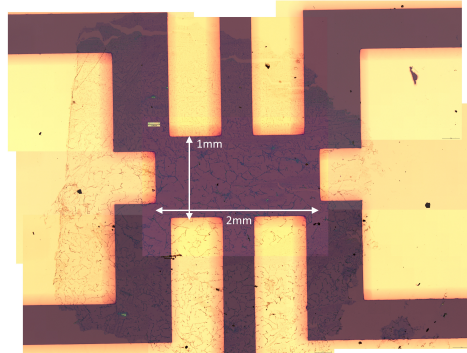


Figure 4.6: Chemical vapour deposition device CVD01

4.3 Temperature & gate dependent conductivity

For two devices, CVD01 and EXF06 I was able to capture a reasonable spread of temperature data to analyse the phonon contributions to graphene's transport properties. The qualitative change in their gate voltage - conductivity (V_gC) curves are shown below.

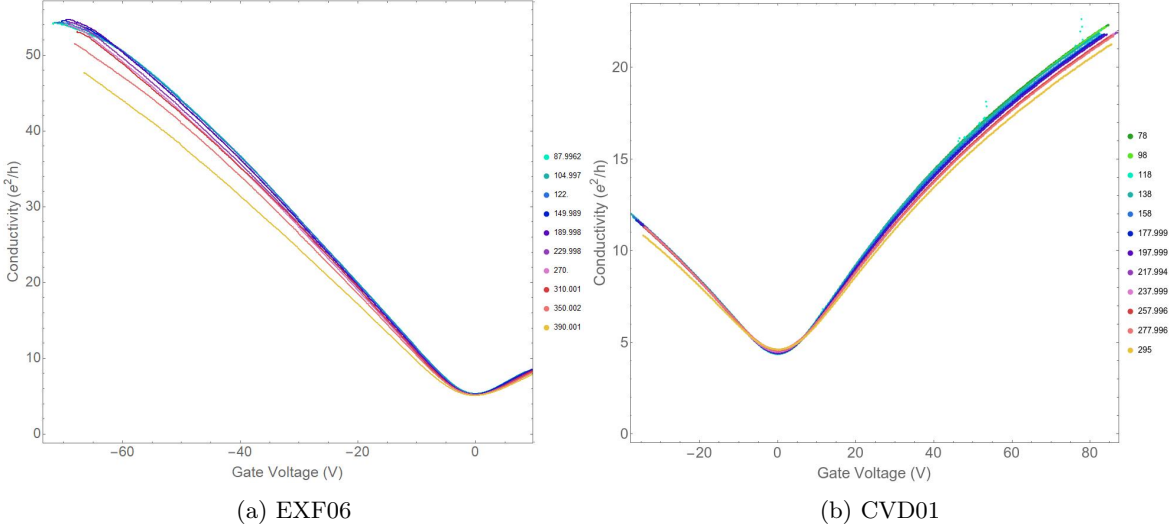


Figure 4.7: Temperature dependence of VgC curves. Here the gate voltages have been shifted so that the Dirac point of each temperature data run is found at 0V.

It is clear that in both CVD01 and EXF06 that as temperature increases, the resistivity of graphene increases, as the slope of the conductivity clearly drops off in higher carrier density.

4.3.1 V_G R mobility

Having fitted eq. (4.7) for each temperature, the fitted mobility parameter can be plotted across temperature. Strictly, $\mu(T, V_g) = \frac{\sigma(V_g, T)}{n(V_g)e}$ such that the mobility should be a function of gate voltage and temperature (see below), however I have found temperature dependent mobility which doesn't consider gate dependence. This is a relevant measure, but not concrete.

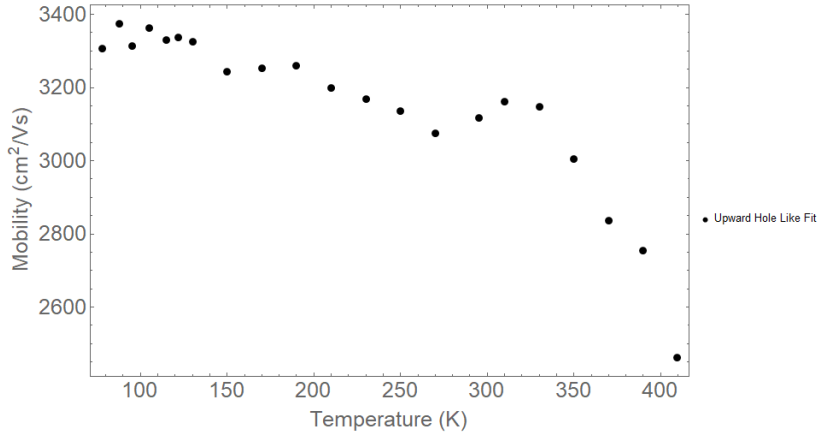


Figure 4.8: Gate voltage vs resistivity temperature dependent mobility for EXF06

At low temperature ($\leq 130K$) LA phonons in graphene are expected to weakly dominate scattering, but at higher temperature remote phonon scattering from SiO_2 is expected to dominate^[21]. This is clear in fig. 4.8, particularly with the steep decent in mobility after 300K.

4.3.2 Temperature dependent conductivity

As described above, a more comprehensive analysis of the conductivity is required to really determine the mobility behaviour. I fit the conductivity across gate voltage and temperature, and show the remote phonon contribution to temperature and gate dependent conductivity.

$$\rho[V_g, T] = \rho_0[V_g] + \rho_A[T] + \rho_B[Vg, T] \quad (4.14)$$

To investigate the contribution of phonons (both longitudinal acoustic and remote polar) to resistivity using the temperature spread of the data taken for devices, my fitting function (eq. (4.14)) comprises of three components. ρ_0 is the intrinsic gate dependent resistivity found near 0K (we have to allow a free parameter R_0 due to not having a measurement near absolute zero), ρ_A is the longitudinal acoustic phonons found within graphene which scales linearly with temperature, and ρ_B is the contribution from remote polar phonons found in SiO₂ affected by both the gating voltage (affecting the polarity) and the temperature (vibrational excitations).

$$\rho_A[T] = \left(\frac{h}{e^2} \right) \frac{\pi 2 D a^2 k_B T}{2 h^2 \rho_s V_s^2 V_F^2} \quad (4.15)$$

$$\rho_B[V_G, T] = B \frac{h}{e^2} V_G^{-\alpha_1} \left(\frac{1}{\exp[(0.059 \text{ eV})/k_B T] - 1} + \frac{6.5}{\exp[(0.115 \text{ eV})/k_B T] - 1} \right) \quad (4.16)$$

For eq. (4.15), k_B is the Boltzmann constant, ρ_s is the 2D mass density of graphene, v_F is the Fermi velocity, v_s is the velocity of sound and D_A is a fitted parameter, the deformation potential. eq. (4.16) is a combination of two surface phonons in SiO₂, given by Bose-Einstein distributions^[21]. These distributions come from the optical phonon energies in SiO₂, at 59 meV and 155 meV^[41].

4.3.2.1 EXF06 - Exfoliated graphene

I used three different fits to observe the presence of these phonons in graphene. The fit parameters in table 4.2 correspond to the curves in fig. 4.9a.

	Estimate	Standard Error	t-Statistic	P-Value		Estimate	Standard Error	t-Statistic	P-Value		Estimate	Standard Error	t-Statistic	P-Value
B1	2.64154	1.04007	2.53977	0.0123489	B1	0.700215	0.0984674	7.11113	4.46888×10^{-11}	B1	0.683172	0.164676	4.14858	0.0000509484
α_1	1.51856	0.177854	8.53824	4.51803×10^{-14}	α_1	1.0069	0.0657146	15.3223	2.03449×10^{-32}	α_1	1.04827	0.114204	9.17889	8.68523×10^{-17}
R0	1.29305	4.87609	0.265181	0.791318	R0	-2.10098	6.7395	-0.311741	0.755673	R0	-5.81577	9.96471	-0.583637	0.560175
Da	-1.76288×10^{-7}	3.79429×10^8	-4.64614×10^{-16}	1	Da	2.84005×10^{-8}	2.79812×10^9	1.01527×10^{-17}	1	Da	1.02356×10^{-6}	1.1093×10^8	9.22711×10^{-15}	1

(a) $T < 270^\circ K$

(b) $T < 270^\circ K, T > 370^\circ K$

(c) $70^\circ K < T < 410^\circ K$

Table 4.2: Phonon fit parameters

Our results for the remote phonon contributions are quite close to that of Chen *et al.*^[21] when I include the upper data (tables 4.2b and 4.2c), with α_1 & B1 parameters ≈ 1.02 & 0.7 respectively, matching 1.04 and 0.6 from Chen *et al.*^[21], showing that the remote phonon contributions can reliably be detected in our devices.

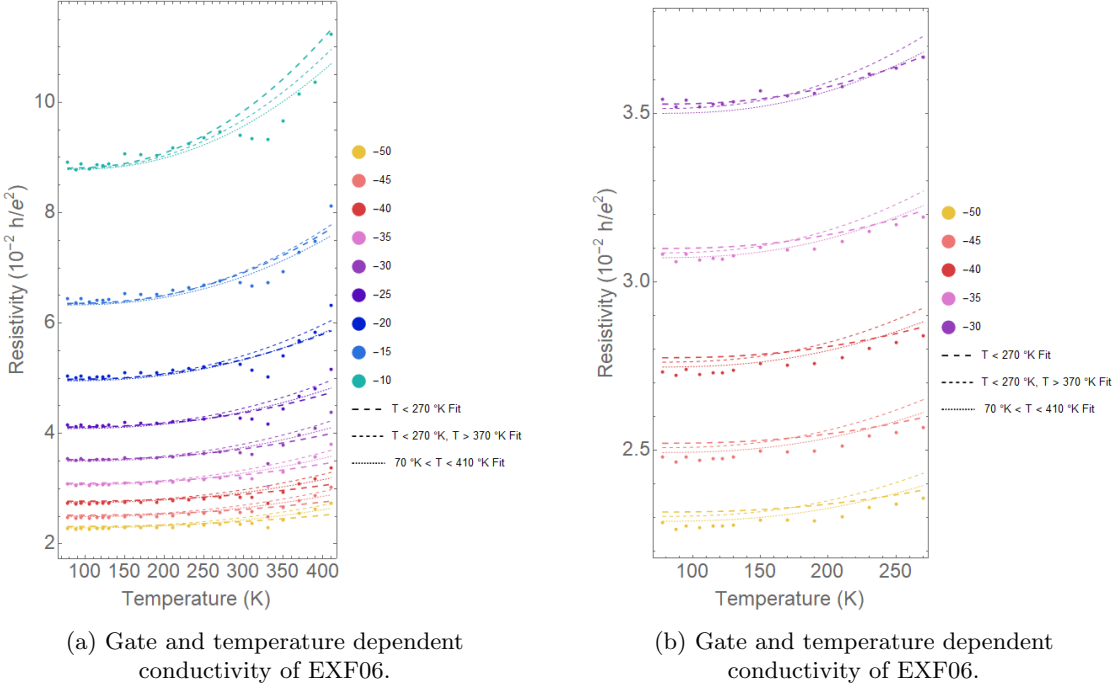
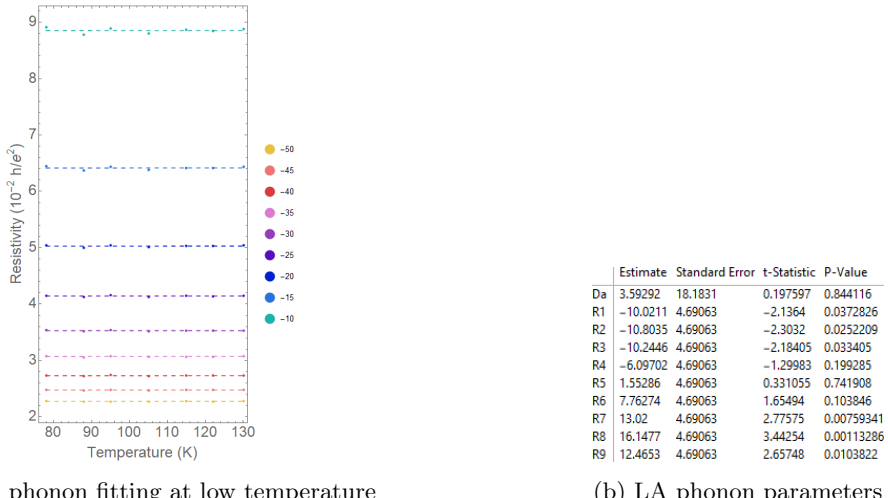


Figure 4.9: Gate and temperature dependence of resistivity for EXF06. 3 fits have been conducted over different domains due to the bump that occurs at about 330 °K

However, the fits for the longitudinal acoustic phonons are very poor, with the D_a parameter not fitting in any of the examples. To attempt to fit to solely the longitudinal acoustic phonon contribution, I took data between 78 °K and 130 °K, reflecting the linear region of the acoustic phonon contribution in Chen *et al*, and removed the remote phonon contribution ρ_B to the fitting function. I also tried adding further freedom in the initial resistance, by adding a free parameter for every gate voltage, in order to observe the longitudinal acoustic phonon contribution.



(a) LA phonon fitting at low temperature

(b) LA phonon parameters

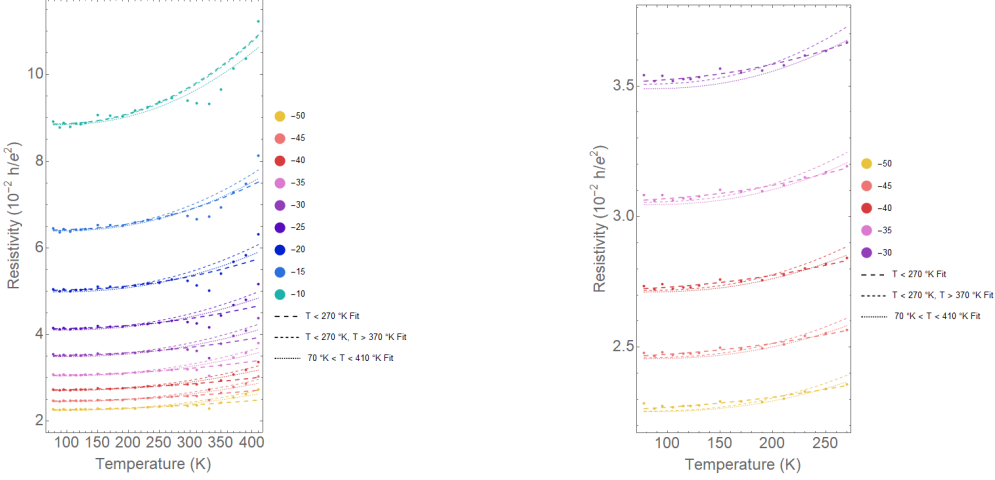
Figure 4.10: Fitting of EXF06 to LA phonons in low temperature data

Figure 4.10 has given the first successful fit to a LA phonon contribution, however the D_a parameter is far from the theoretical prediction seen in Chen *et al.*^[21] at 18 eV, significantly reducing any contribution. The data is visually unconvincing in linear gradient at this scale. I have also attempted to fit the full resistivity contribution again using the extra freedom in the offset resistance parameters in

	Estimate	Standard Error	t-Statistic	P-Value		Estimate	Standard Error	t-Statistic	P-Value		Estimate	Standard Error	t-Statistic	P-Value		
B1	2.5872	0.850448	3.04216	0.00291558		B1	0.542092	0.0724826	7.47893	7.29123×10^{-12}		B1	0.520103	0.137898	3.77165	0.000220917
a1	1.61288	0.146077	11.0413	1.02186×10^{-19}		a1	0.94351	0.0603954	15.305	9.07788×10^{-32}		a1	0.960511	0.120759	7.95396	2.06539×10^{-13}
Da	13.9841	2.68318	5.21177	8.42279×10^{-7}		Da	-2.31216 $\times 10^{-9}$	3.19844 $\times 10^0$	-7.22903 $\times 10^{-20}$	1		Da	-2.98458 $\times 10^{-7}$	4.0379 $\times 10^8$	-7.39142×10^{-16}	1
R1	-16.741	3.416	-4.90074	3.18671×10^{-6}		R1	-14.5456	7.91501	-1.83772	0.0682081		R1	-15.1449	13.3168	-1.13728	0.256958
R2	-17.0851	3.35476	-5.09279	1.40899×10^{-6}		R2	-14.3789	7.81851	-1.83900	0.0680066		R2	-15.4873	13.1	-1.18224	0.238695
R3	-16.3256	3.28198	-4.97433	2.33596×10^{-6}		R3	-13.4966	7.71261	-1.74993	0.0823058		R3	-15.0067	12.8614	-1.1668	0.244859
R4	-12.4774	3.19505	-3.90521	0.000159948		R4	-9.92671	7.59725	-1.30662	0.193469		R4	-12.5679	12.6005	-0.997411	0.319927
R5	-5.55929	3.09138	-1.79832	0.0747726		R5	-3.95527	7.47437	-0.529177	0.597515		R5	-8.54596	12.3209	-0.693613	0.488834
R6	1.28444	2.97038	0.432415	0.666257		R6	2.62481	7.35258	0.356992	0.721631		R6	-2.02985	12.0408	-0.168581	0.866319
R7	7.5939	2.84226	2.67178	0.00864999		R7	8.74784	7.2632	1.20441	0.23045		R7	1.92017	11.8299	0.162315	0.871243
R8	11.6176	2.77917	4.18024	0.000057366		R8	14.3073	7.33232	1.95127	0.0530079		R8	10.0357	11.9837	0.837439	0.403475
R9	9.17665	3.44139	2.66656	0.0087775		R9	14.9949	8.22153	1.82386	0.0702905		R9	9.07	14.1145	0.6426	0.521315

(a) $T < 270^\circ K$ (b) $T < 270^\circ K, T > 370^\circ K$ (c) $70^\circ K < T < 410^\circ K$

Table 4.3: Gate and temperature dependence of resistivity fit parameters for EXF06 but with each gate voltage having a scalar-resistance degree of freedom.



(a) Gate and temperature dependent conductivity of EXF06.
(b) Gate and temperature dependent conductivity of EXF06.

Figure 4.11: Gate and temperature dependence of resistivity for EXF06. 3 fits have been conducted over different domains due to the bump that occurs at about $330^\circ K$. Each gate voltage has a scalar resistance degree of freedom.

Lastly, the fits of fig. 4.11a and table 4.3 successfully fit to a reasonable LA phonon contribution ($D_a \rightarrow 13.9 \pm 2.7$ eV) in the subset of data under the temperature of $270^\circ K$. This is a little more convincing, but likely just fitting to the remote phonon contribution past $130^\circ K$.

There are a few good possible reasons as to why EXF06 did not see clearly see the longitudinal acoustic phonons from graphene. Firstly, there is a big kink in the temperature dependent curve at all gate voltages. I suspect that this was due to the fact that this sample was cooled to about $150^\circ K$ before the turbo pump was activated. It is highly likely that adsorbates condensed on the surface of the graphene that we were measuring, affecting the amount of trapped charges and

impurities and increasing scattering on graphene. It becomes clear then that if this condensed material evaporates around room temperature, the conductivity would increase as seen, before the remote phonon contribution outscales any gains made by evaporation of absorbates. It is unclear when the evaporation begins however, and this could completely mask evidence of longitudinal acoustic phonons.

Additionally to the point, the data acquired by Chen *et al* is taken in ultra high vacuum (UHV) at about 10^{-10} mBar which would provide an extremely clean environment, compared to our turbo pump at 10^{-5} mBar.

Secondly, the gated mobility of this device was around $0.33 \text{ m}^2/\text{Vs}$, which is comparably low to other exfoliated devices with around $1.6 \text{ m}^2/\text{Vs}$. As a result, the gate-voltage dependent resistivity isn't as sharp. Sharpness is desired to add spread in temperature measurements, where small phonon contributions might be more easily identified. This isn't as significant as the effect of absorbates, but still relevant.

Finally, we can use the parameter set in table 4.2b to determine the mobility in eq. (4.17).

$$\mu [V_g, T] = \frac{\sigma [V_g, T]}{N [V_g] \times e} \quad (4.17)$$

Plotting for a few different gate voltages in fig. 4.12, there's general consistency and agreement between the gate-voltage mobility and the full temperature-gate-voltage dependent mobility:

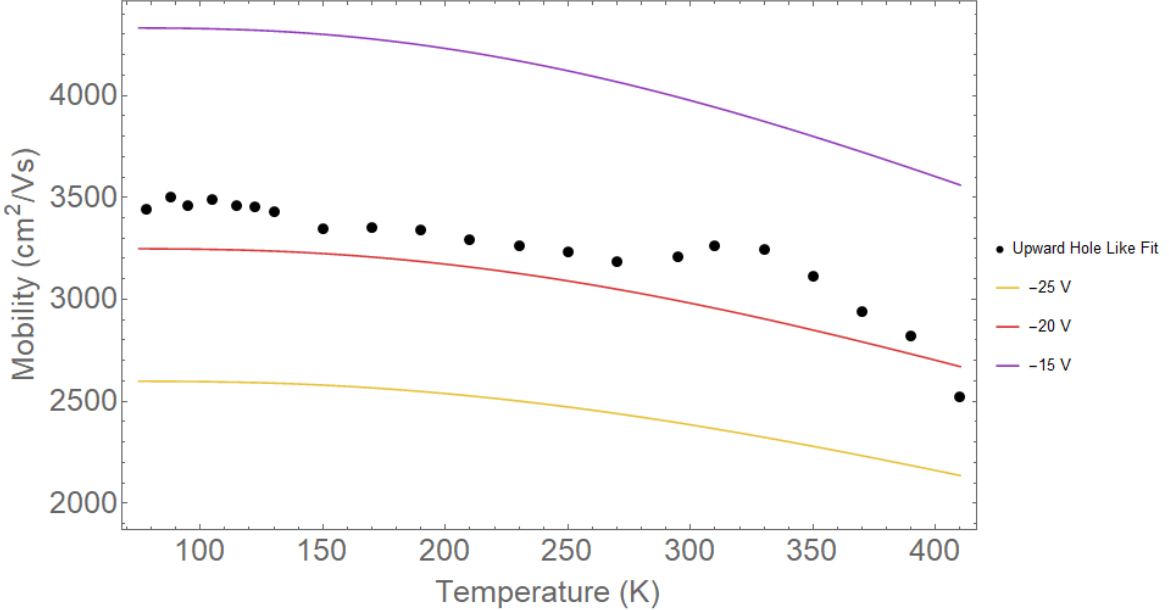


Figure 4.12: EXF06 temp. & V_g dependent mobility

4.3.3 hBN transfer

Chapter 5

Thin oxides

In this chapter, I explore various liquid metal stamping techniques^[22] that were further developed through my work to transfer oxides on a graphene device. Progress towards successful oxide transfer was achieved by using many dummy devices consisting of gold pads but no device.

During this time I worked closely with Kourosh Kalantar-zadeh's group at RMIT (Royal Melbourne institute of technology), in particular Ali Zavabeti, Torben Daeneke, Nitu Syed, Hareem Khan and Paul Atkin in developing this work.

5.1 Printing

The traditional technique of mechanical exfoliation is at the core creating many new materials in current research. This is also the case with the liquid metal stamping technique. In this section, I will discuss Al_2O_3 , SnO and Bi_2O_3 , all of which are synthesised by 'stamping' onto liquid metal droplets.

5.1.1 Al_2O_3

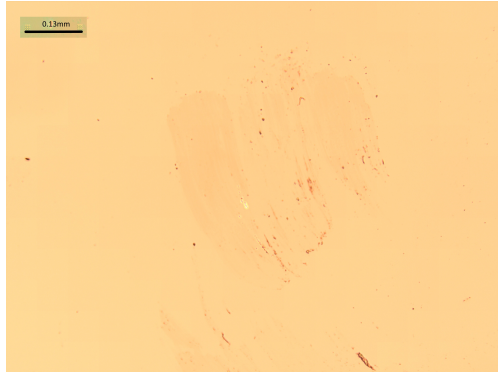
Aluminium oxide was the first oxide Ali and I investigated for use in our devices. This was for the reason that generally Al_2O_3 is very easy to make by grinding up aluminium wire. I have already detailed the bare process in section 2.1.10. An example of the droplets created using the mortar and pestle is seen in fig. 5.1, and the touching process.



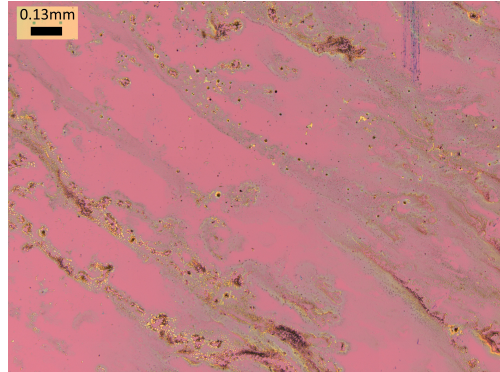
Figure 5.1: Synthesis process for stamping Al_2O_3

We tested over 30 samples on droplets, varying radii and exposure time to air (to let the oxide

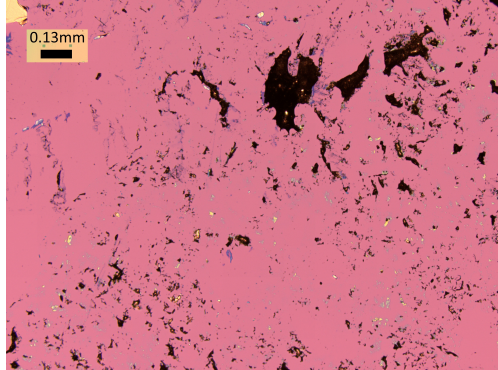
form on the surface). Unfortunately very little material transferred in any of these tests, with only one clean deposition as shown in fig. 5.2a.



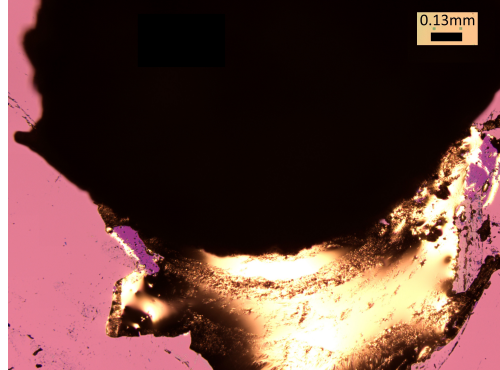
(a) AlO_3 on SiO_2 (unknown thickness).



(b) Non uniform oxide deposition, but some thin areas



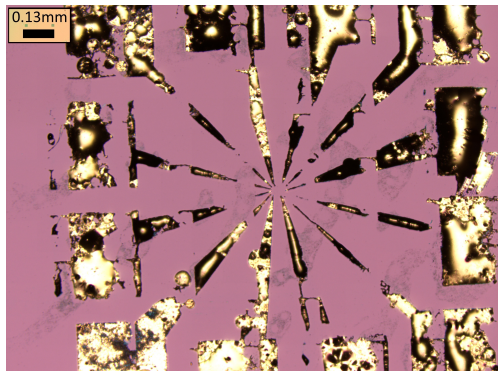
(c) Metal residue left after an unsuccessful transfer



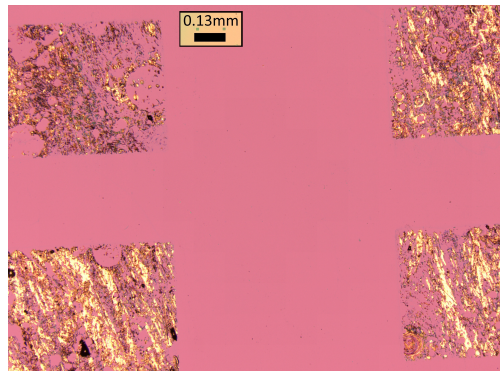
(d) Metal remaining, with traces of thick (gallium) oxide

Figure 5.2: Deposition of AlO_3 onto SiO_2 . Scale bar: 0.13mm

More commonly than not though, the liquid metal begun interacting with gold pads and adhering through any oxide layer, or no oxide was deposited (fig. 5.3)



(a) Adhesion of gallium to gold pads



(b) After cleaning off gallium, remains of gold pads

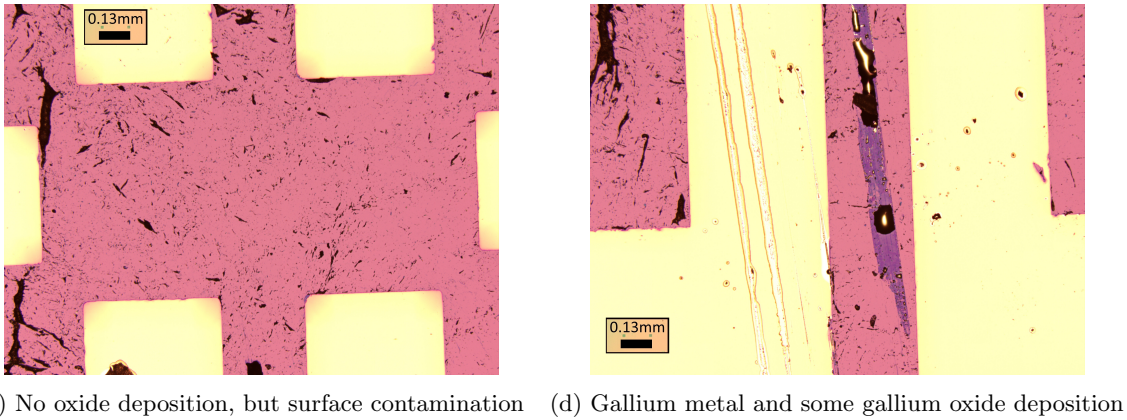


Figure 5.3: Deposition of AlO_3 onto Au on SiO_2

We also attempted spreading oxide on transferred CVD graphene, but no evidence of oxide transfer was found optically (fig. 5.4).

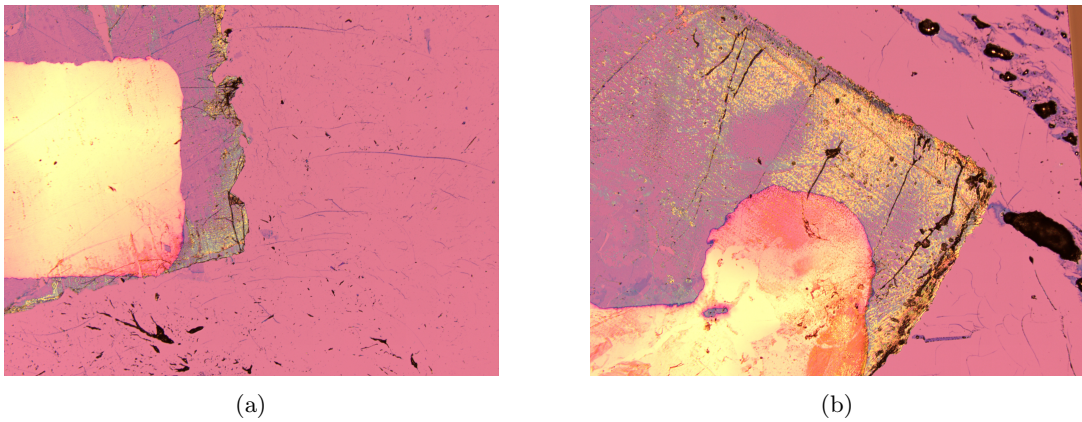


Figure 5.4: Contamination of CVD graphene without transfer of AlO_3 .

After three trials using aluminium oxide and varying the exfoliation method, Torben suggested we try some other oxides for something more reliable and clean, particularly for the time window of this project.

5.1.2 SnO & Bi_2O_3

After switching from AlO_3 , I tried to start using SnO , Bi_2O_3 and GaO_3 (see section 5.2 below). Hareem assisted me with transferring Bi_2O_3 and SnO onto desired substrates, using the same base method of exfoliation in a low oxygen fumehood, but with a few modifications.

Different from AlO_3 , we used pure tin and bismuth (no need for a gallium alloy) and melted the chunks on a hotplate at 330°C and 270°C respectively. We also used glass slides to ‘sacrifice’ a layer of outer material before proceeding to attempt to exfoliate a layer of material.

We had immediate success with this method for depositing onto bare substrates, as seen in fig. 5.5.

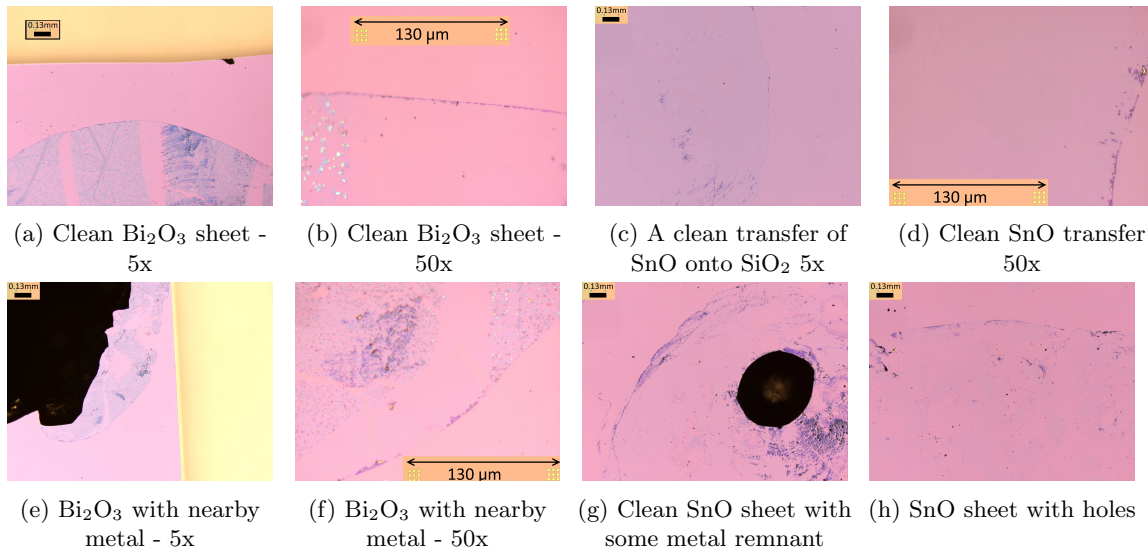


Figure 5.5: Deposition of Bi_2O_3 and SnO onto SiO_2 . Scale bar: 0.13mm

Sheets are much more uniform and easy to come by than that of AlO_3 . Unfortunately it was still clear (fig. 5.6) that, for both bismuth and tin metals, adhesion to gold contacts was still a significant problem and resulted in very little oxide transfer. This is likely due to the breaking of the thin oxides surface during contact and interaction thereafter of metals.

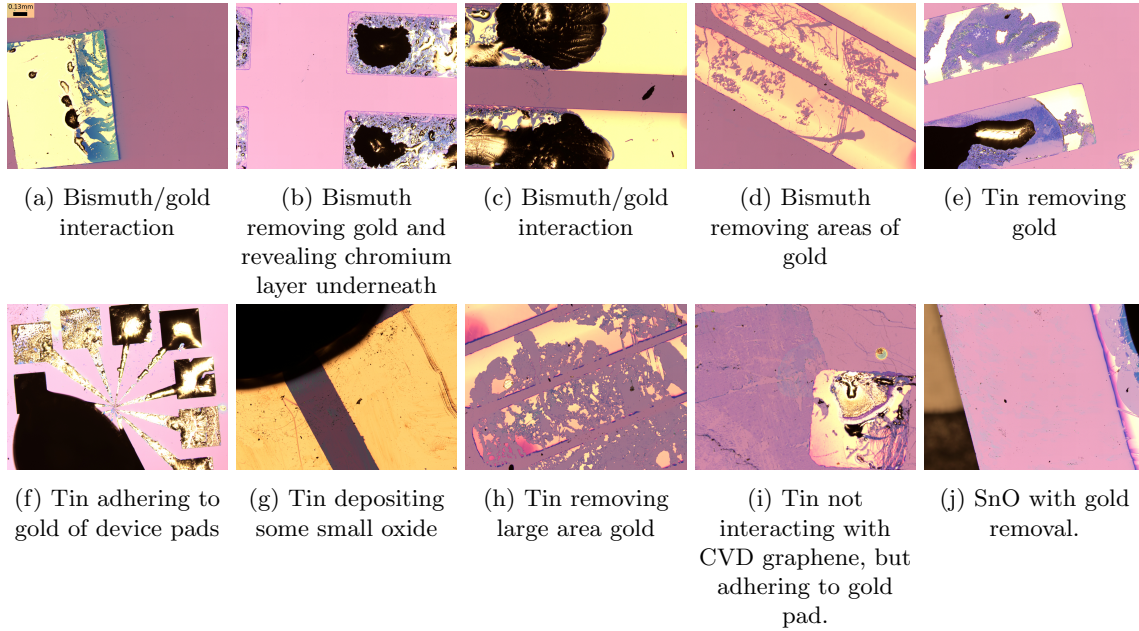


Figure 5.6: Strong gold bismuth/tin interaction. All images with same scalebar as fig. 5.6a, 130 μm .

5.2 Smearing Ga_2O_3

5.2.1 Devices

Chapter 6

Conclusion

6.1 Future direction

6.2 Concluding remarks

List of Figures

2.1	Process diagram for device fabrication	8
2.2	CVD graphene grown on Cu transferred onto SiO ₂ and Au pads.	8
2.3	Spin curve of AZ-1512HS	10
2.4	Material remanants from lithography	11
2.5	Bilayer lithography process	11
2.6	Photolithography mask writing	12
2.7	Developing an exposure array on SiO ₂	12
2.8	Cleaning of graphene using UV Ozone	13
2.9	E-beam evaporation	13
2.10	Deposition contacts	14
2.11	PG Remover liftoff.	14
2.12	Ultrasonication used to remove material remnants from lithography.	15
2.13	Ultrasonication that has broken graphene sample.	15
2.14	Ag/H annealing	15
2.15	PCB wafter mount	15
2.16	Liquid metal oxide exfoliation	16
2.17	Schematics of resistance measurements	17
2.18	Instrumentation connections to a gated graphene FET	18
2.19	LakeShore Probestation	19
2.20	Probestation refrigerator	20
2.21	Probestation micro-manipulated stages	21
3.1	Ratio of G to 2D peaks in graphene and bilayer	23
3.2	Raman 2D fitting of graphene and bilayer	24
3.3	Raman processes in graphene	24
3.4	RGB images of graphene on 285nm SiO ₂	25
3.5	Contrast imaging sample 1	26
3.6	Contrast imaging sample 2	26
4.1	Two equivalent geometries of trapezoids.	27
4.2	EXF06 Geometry	28
4.3	EXF04 Geometry	28
4.4	Gate dependent transport of EXF06	29
4.5	Geometric factor fitting to find \mathcal{N}	30
4.6	Device CVD01	31
4.7	Changes in gate-voltage conductivity with temperature	32
4.8	Gate voltage vs resistivity temperature dependent mobility for EXF06	32
4.9	Gate and temperature dependence of resistivity for EXF06	34
4.10	EXF06 LA phonon fitting	34

4.11	Gate and temperature dependence of resistivity for EXF06 with R flexibility	35
4.12	EXF06 temp. & V_g dependent mobility	36
5.1	AlO ₃ synthesis process	37
5.2	AlO ₃ stamped on SiO ₂	38
5.3	AlO ₃ stamped on SiO ₂	39
5.4	AlO ₃ stamped on CVD graphene & SiO ₂	39
5.5	Bi ₂ O ₃ and SnO stamped on SiO ₂	40
5.6	Strong gold bismuth/tin interaction	40

List of Tables

4.1	Geometric factor fitting to find μ	30
4.2	Phonon fit parameters	33
4.3	Gate and temperature dependence of resistivity fit parameters for EXF06 with R flexibility	35
B.1	Table 1 - Theoretical values of impurities in graphene relating to other parameters. . .	60

Chapter 7

Bibliography

- [1] K. S. Novoselov, A. K. Geim, S. V. Morozov, D. Jiang, Y. Zhang, S. V. Dubonos, I. V. Grigorieva, and A. A. Firsov. Electric Field Effect in Atomically Thin Carbon Films. *Science*, 306(5696):666–669, October 2004.
- [2] Yi Zhang, Luyao Zhang, and Chongwu Zhou. Review of Chemical Vapor Deposition of Graphene and Related Applications. *Accounts of Chemical Research*, 46(10):2329–2339, October 2013.
- [3] K. S. Novoselov, D. Jiang, F. Schedin, T. J. Booth, V. V. Khotkevich, S. V. Morozov, and A. K. Geim. Two-dimensional atomic crystals. *Proceedings of the National Academy of Sciences*, 102(30):10451–10453, July 2005.
- [4] Xuesong Li, Weiwei Cai, Jinho An, Seyoung Kim, Junghyo Nah, Dongxing Yang, Richard Piner, Aruna Velamakanni, Inhwa Jung, Emanuel Tutuc, Sanjay K. Banerjee, Luigi Colombo, and Rodney S. Ruoff. Large-Area Synthesis of High-Quality and Uniform Graphene Films on Copper Foils. *Science*, 324(5932):1312–1314, June 2009.
- [5] Claire Berger, Zhimin Song, Tianbo Li, Xuebin Li, Asmerom Y. Ogbazghi, Rui Feng, Zhenting Dai, Alexei N. Marchenkov, Edward H. Conrad, Phillip N. First, and Walt A. de Heer. Ultrathin Epitaxial Graphite: 2d Electron Gas Properties and a Route toward Graphene-based Nanoelectronics. *The Journal of Physical Chemistry B*, 108(52):19912–19916, December 2004.
- [6] J. Hass, R. Feng, T. Li, X. Li, Z. Zong, W. A. de Heer, P. N. First, E. H. Conrad, C. A. Jeffrey, and C. Berger. Highly ordered graphene for two dimensional electronics. *Applied Physics Letters*, 89(14):143106, October 2006.
- [7] Changxi Zheng, Qianhui Zhang, Bent Weber, Hesameddin Ilatikhameneh, Fan Chen, Harshad Sahasrabudhe, Rajib Rahman, Shiqiang Li, Zhen Chen, Jack Hellerstedt, Yupeng Zhang, Wen Hui Duan, Qiaoliang Bao, and Michael S. Fuhrer. Direct Observation of 2d Electrostatics and Ohmic Contacts in Template-Grown Graphene/WS₂ Heterostructures. *ACS Nano*, 11(3):2785–2793, March 2017.
- [8] Microchem.com (2001). Nano remover pg, 2001.
- [9] Yuan Huang, Eli Sutter, Norman N. Shi, Jiabao Zheng, Tianzhong Yang, Dirk Englund, Hong-Jun Gao, and Peter Sutter. Reliable Exfoliation of Large-Area High-Quality Flakes of Graphene and Other Two-Dimensional Materials. *ACS Nano*, 9(11):10612–10620, November 2015.
- [10] Az1500 series technical datasheet.
- [11] EMD performance materials. Az 1500 series technical datasheet.

- [12] Jeongwon Park, Richard D. Yang, Corneliu N. Colesniuc, Amos Sharoni, Sungho Jin, Ivan K. Schuller, William C. Trogler, and Andrew C. Kummel. Bilayer processing for an enhanced organic-electrode contact in ultrathin bottom contact organic transistors. *Applied Physics Letters*, 92(19):193311, May 2008.
- [13] Microchem.com (2018). Pmgi and lor resists: Faqs :: Microchem., 2018.
- [14] Wei Li, Yiran Liang, Dangmin Yu, Lianmao Peng, Kurt P. Pernstich, Tian Shen, A. R. Hight Walker, Guangjun Cheng, Christina A. Hacker, Curt A. Richter, Qiliang Li, David J. Gundlach, and Xuelei Liang. Ultraviolet/ozone treatment to reduce metal-graphene contact resistance. *Applied Physics Letters*, 102(18):183110, May 2013.
- [15] A. Nath, A. D. Koehler, G. G. Jernigan, V. D. Wheeler, J. K. Hite, S. C. Hernndez, Z. R. Robinson, N. Y. Garces, R. L. Myers-Ward, C. R. Eddy, D. K. Gaskill, and M. V. Rao. Achieving clean epitaxial graphene surfaces suitable for device applications by improved lithographic process. *Applied Physics Letters*, 104(22):224102, June 2014.
- [16] Anindya Nath, Marc Currie, Anthony K. Boyd, Virginia D. Wheeler, Andrew D. Koehler, Marko J. Tadjer, Zachary R. Robinson, Karthik Sridhara, Sandra C. Hernandez, James A. Wollmershauser, Jeremy T. Robinson, Rachael L. Myers-Ward, Mulpuri V. Rao, and D. Kurt Gaskill. In search of quantum-limited contact resistance: understanding the intrinsic and extrinsic effects on the graphenemetal interface. *2D Materials*, 3(2):025013, 2016.
- [17] Understanding Thin Film Process TechnologiesREO Inc.
- [18] Yung-Chang Lin, Chun-Chieh Lu, Chao-Huei Yeh, Chuanhong Jin, Kazu Suenaga, and Po-Wen Chiu. Graphene Annealing: How Clean Can It Be? *Nano Letters*, 12(1):414–419, January 2012.
- [19] Daniel R. Cooper, Benjamin DAnjou, Nageswara Ghattamaneni, Benjamin Harack, Michael Hilke, Alexandre Horth, Norberto Majlis, Mathieu Massicotte, Leron Vandsburger, Eric Whiteman, and Victor Yu. Experimental Review of Graphene, 2012.
- [20] Caterina Soldano, Ather Mahmood, and Erik Dujardin. Production, properties and potential of graphene. *Carbon*, 48(8):2127–2150, July 2010.
- [21] Jian-Hao Chen, Chaun Jang, Shudong Xiao, Masa Ishigami, and Michael S. Fuhrer. Intrinsic and extrinsic performance limits of graphene devices on SiO₂. *Nature Nanotechnology*, 3(4):206–209, April 2008.
- [22] Ali Zavabeti, Jian Zhen Ou, Benjamin J. Carey, Nitu Syed, Rebecca Orrell-Trigg, Edwin L. H. Mayes, Chenglong Xu, Omid Kavehei, Anthony P. OMullane, Richard B. Kaner, Kourosh Kalantar-zadeh, and Torben Daeneke. A liquid metal reaction environment for the room-temperature synthesis of atomically thin metal oxides. *Science*, 358(6361):332–335, October 2017.
- [23] Keithley Instruments. *Model 2400 Series SourceMeter User's Manual*, 2400s-900-01 rev. g edition, May 2002.
- [24] Stanford Research Systems. *Model SR830 DSP Lock-In Amplifier*, 2.5 edition, October 2011.
- [25] Richard F. Voss and John Clarke. Flicker ($\frac{1}{f}$) noise: Equilibrium temperature and resistance fluctuations. *Physical Review B*, 13(2):556–573, January 1976.
- [26] F.N. Hooge. 1/f noise sources. *IEEE Transactions on Electron Devices*, 41(11):1926–1935, November 1994.

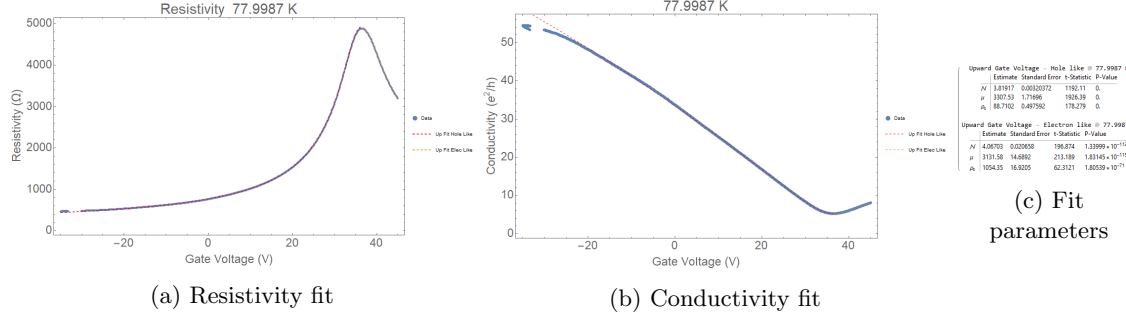
- [27] R. P. Vidano, D. B. Fischbach, L. J. Willis, and T. M. Loehr. Observation of Raman band shifting with excitation wavelength for carbons and graphites. *Solid State Communications*, 39(2):341–344, July 1981.
- [28] R. J. Nemanich and S. A. Solin. First- and second-order Raman scattering from finite-size crystals of graphite. *Physical Review B*, 20(2):392–401, July 1979.
- [29] F. Tuinstra and J.L. Koenig. Characterization of Graphite Fiber Surfaces with Raman Spectroscopy. *Journal of Composite Materials*, 4(4):492–499, October 1970.
- [30] F. Tuinstra and J. L. Koenig. Raman Spectrum of Graphite. *The Journal of Chemical Physics*, 53(3):1126–1130, August 1970.
- [31] A. C. Ferrari, J. C. Meyer, V. Scardaci, C. Casiraghi, M. Lazzeri, F. Mauri, S. Piscanec, D. Jiang, K. S. Novoselov, S. Roth, and A. K. Geim. Raman Spectrum of Graphene and Graphene Layers. *Physical Review Letters*, 97(18):187401, October 2006.
- [32] Andrea C. Ferrari and Denis M. Basko. Raman spectroscopy as a versatile tool for studying the properties of graphene. *Nature Nanotechnology*, 8(4):235–246, April 2013.
- [33] P. Blake, K. S. Novoselov, A. H. Castro Neto, D. Jiang, R. Yang, T. J. Booth, A. K. Geim, and E. W. Hill. Making graphene visible. *Applied Physics Letters*, 91(6):063124, August 2007. arXiv: 0705.0259.
- [34] Hai Li, Jumiati Wu, Xiao Huang, Gang Lu, Jian Yang, Xin Lu, Qihua Xiong, and Hua Zhang. Rapid and Reliable Thickness Identification of Two-Dimensional Nanosheets Using Optical Microscopy. *ACS Nano*, 7(11):10344–10353, November 2013.
- [35] Ying Ying Wang, Ren Xi Gao, Zhen Hua Ni, Hui He, Shu Peng Guo, Huan Ping Yang, Chun Xiao Cong, and Ting Yu. Thickness identification of two-dimensional materials by optical imaging. *Nanotechnology*, 23(49):495713, 2012.
- [36] R. R. Nair, P. Blake, A. N. Grigorenko, K. S. Novoselov, T. J. Booth, T. Stauber, N. M. R. Peres, and A. K. Geim. Fine Structure Constant Defines Visual Transparency of Graphene. *Science*, 320(5881):1308–1308, June 2008.
- [37] A. B. Kuzmenko, E. van Heumen, F. Carbone, and D. van der Marel. Universal Optical Conductance of Graphite. *Physical Review Letters*, 100(11):117401, March 2008.
- [38] Z. H. Ni, H. M. Wang, J. Kasim, H. M. Fan, T. Yu, Y. H. Wu, Y. P. Feng, and Z. X. Shen. Graphene Thickness Determination Using Reflection and Contrast Spectroscopy. *Nano Letters*, 7(9):2758–2763, September 2007.
- [39] Shaffique Adam, E. H. Hwang, V. M. Galitski, and S. Das Sarma. A self-consistent theory for graphene transport. *Proceedings of the National Academy of Sciences*, 104(47):18392–18397, November 2007.
- [40] Y.-W. Tan, Y. Zhang, K. Bolotin, Y. Zhao, S. Adam, E. H. Hwang, S. Das Sarma, H. L. Stormer, and P. Kim. Measurement of Scattering Rate and Minimum Conductivity in Graphene. *Physical Review Letters*, 99(24):246803, December 2007.
- [41] S. Fratini and F. Guinea. Substrate-limited electron dynamics in graphene. *Physical Review B*, 77(19):195415, May 2008.

Appendices

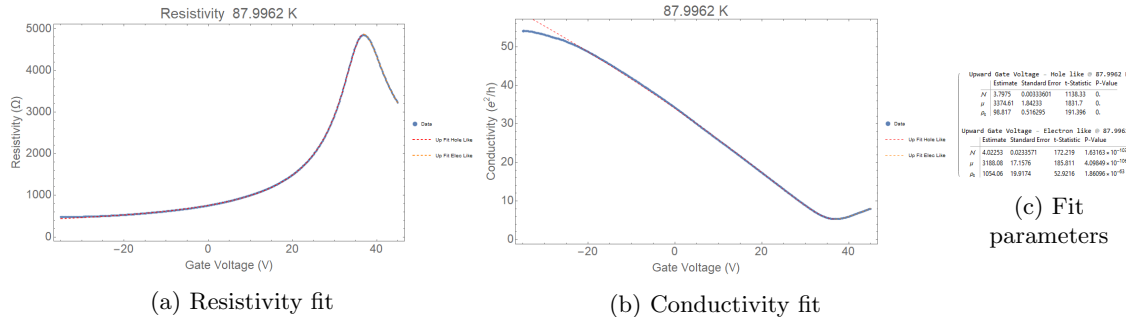
Appendix A

Gate voltage conductivity fits

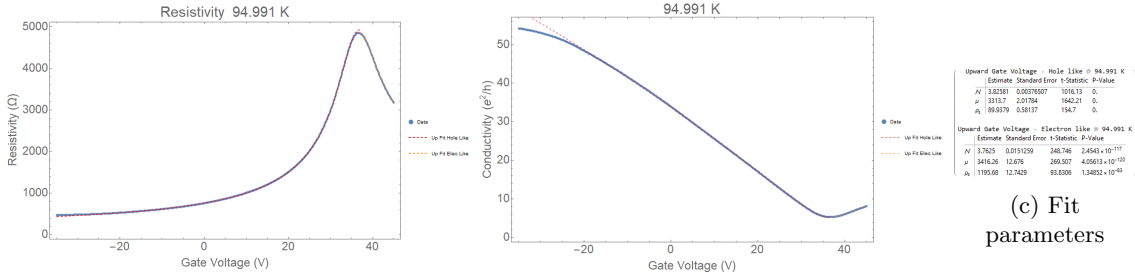
A.1 EXF06 Fits



Gate dependent transport of EXF06 at 78K



Gate dependent transport of EXF06 at 85K

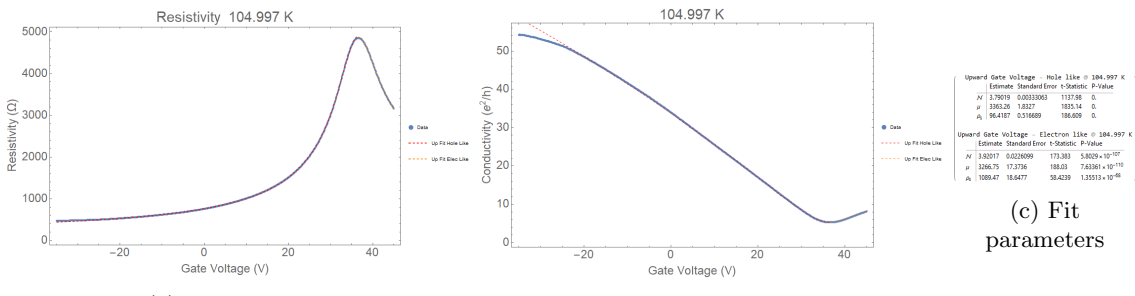


(a) Resistivity fit

(b) Conductivity fit

(c) Fit parameters

Gate dependent transport of EXF06 at 95K

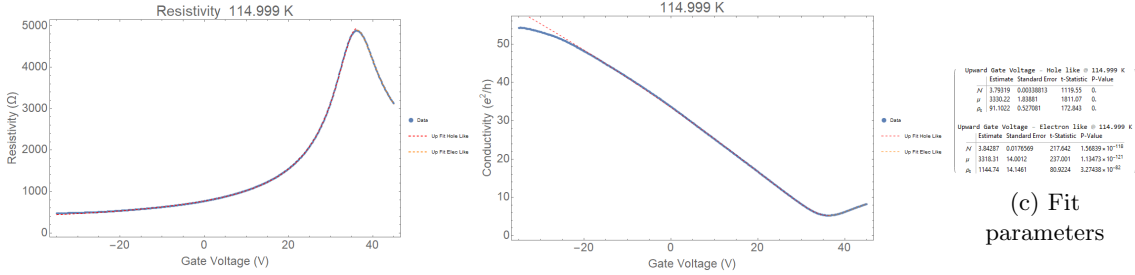


(a) Resistivity fit

(b) Conductivity fit

(c) Fit parameters

Gate dependent transport of EXF06 at 105K

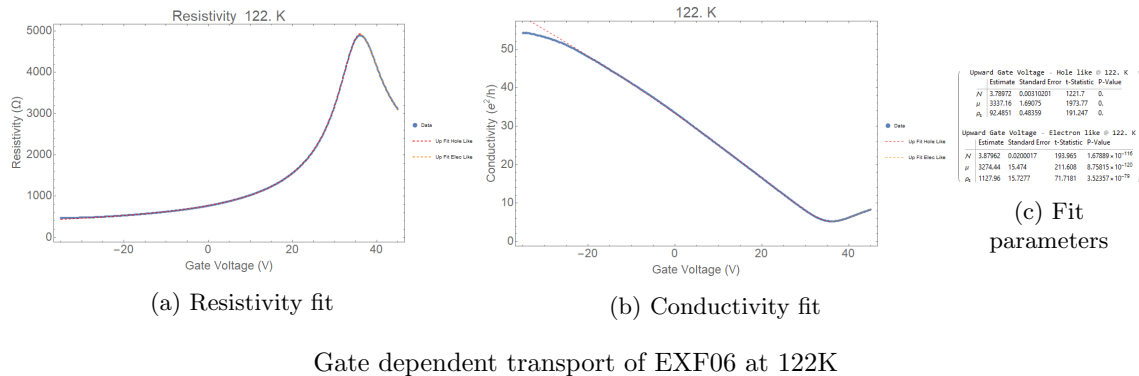


(a) Resistivity fit

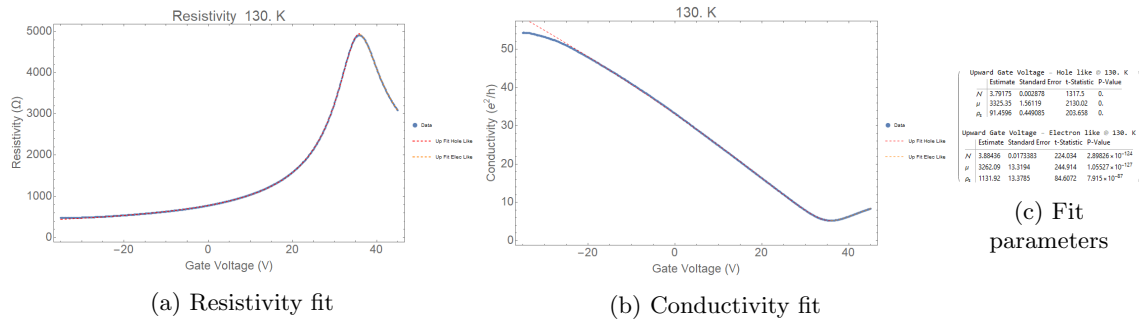
(b) Conductivity fit

(c) Fit parameters

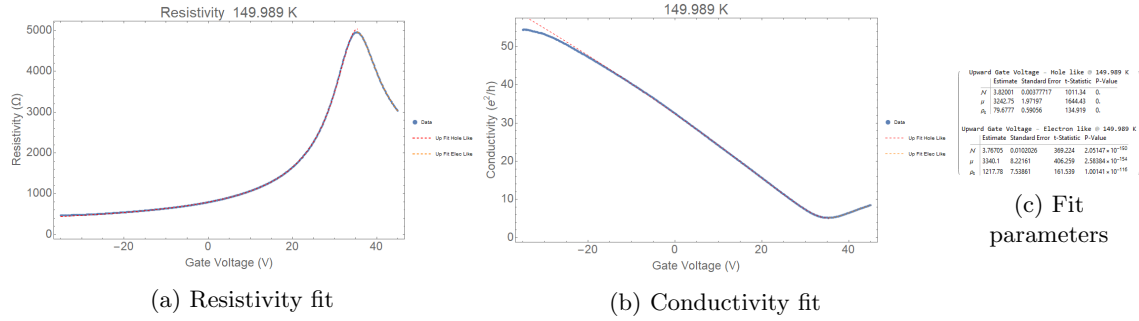
Gate dependent transport of EXF06 at 115K



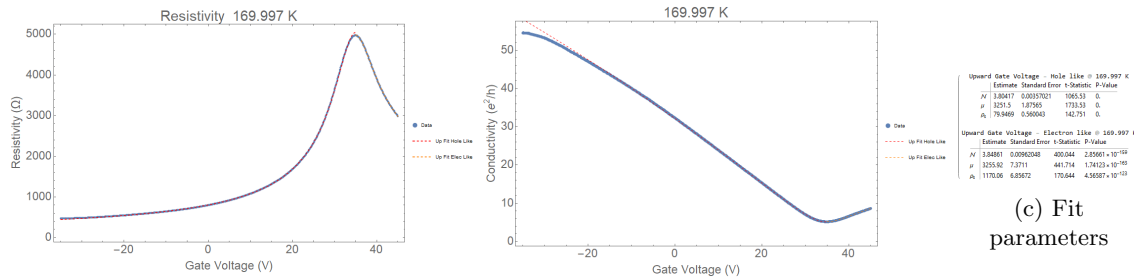
Gate dependent transport of EXF06 at 122K



Gate dependent transport of EXF06 at 130K



Gate dependent transport of EXF06 at 150K



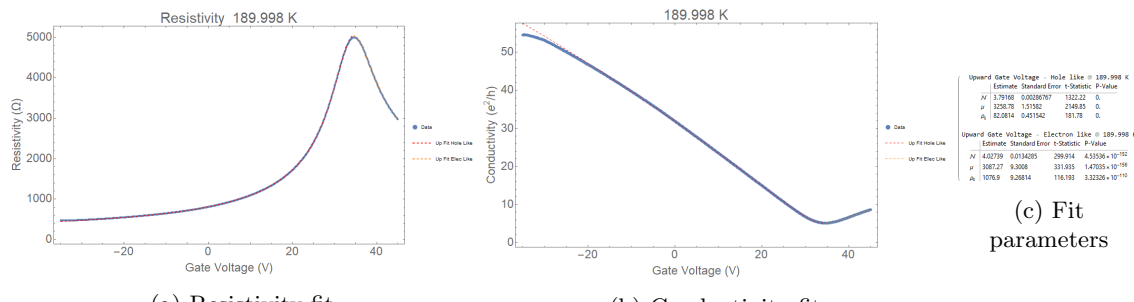
(a) Resistivity fit

(b) Conductivity fit

(c) Fit parameters

Upward Gate Voltage	Hole like	= 169.997 K	
Estimate	StandardError	t-Statistic P-Value	
N	3.804617	0.02037021	1065.53 0.
μ	1.21	0.787604	1735.22 0.
ρ_0	75.8669	5.664004	142.791 0.
A_0	1170.06	6.85072	170.044 4.30087 * 10^-13

Gate dependent transport of EXF06 at 170K



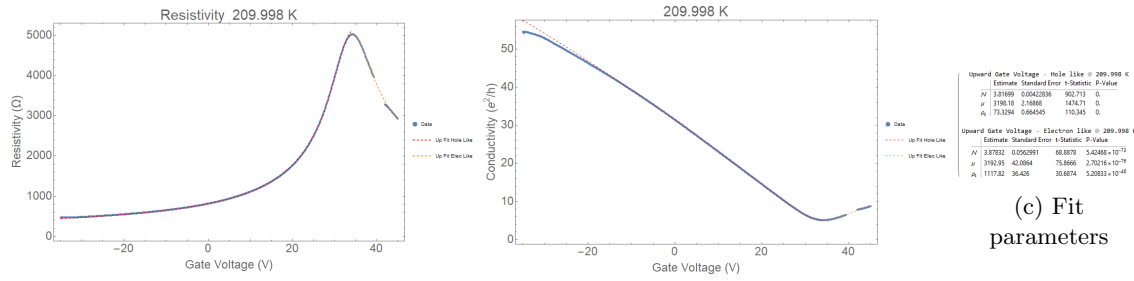
(a) Resistivity fit

(b) Conductivity fit

(c) Fit parameters

Upward Gate Voltage	Hole like	= 189.998 K	
Estimate	StandardError	t-Statistic P-Value	
N	1.7916	0.02369707	1325.22 0.
μ	3258.78	1.51582	2148.85 0.
ρ_0	82.0314	6.051542	181.73 0.
A_0	1076.9	9.26814	116.393 3.32326 * 10^-13

Gate dependent transport of EXF06 at 190K



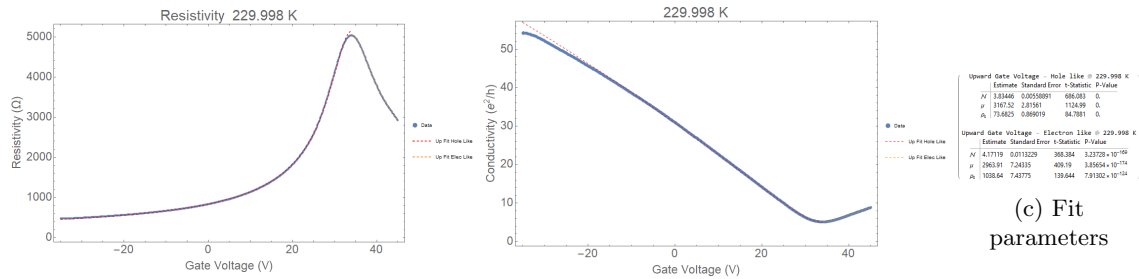
(a) Resistivity fit

(b) Conductivity fit

(c) Fit parameters

Upward Gate Voltage	Hole like	= 209.998 K	
Estimate	StandardError	t-Statistic P-Value	
N	3.81699	0.02422038	902.713 0.
μ	1.21	0.787604	1735.22 0.
ρ_0	73.8294	5.664545	110.32 0.
A_0	1177.32	36.426	30.8674 5.20881 * 10^-13

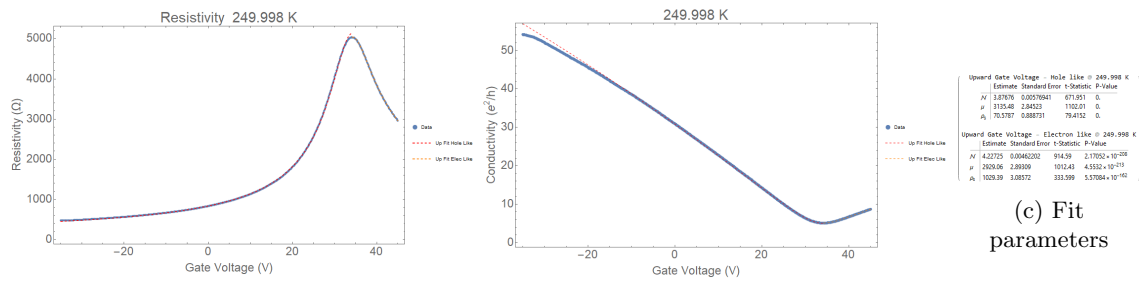
Gate dependent transport of EXF06 at 210K



(a) Resistivity fit

(b) Conductivity fit

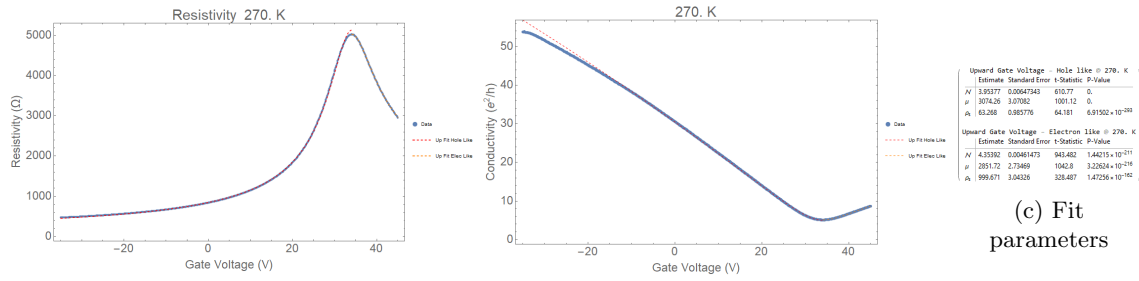
Gate dependent transport of EXF06 at 230K



(a) Resistivity fit

(b) Conductivity fit

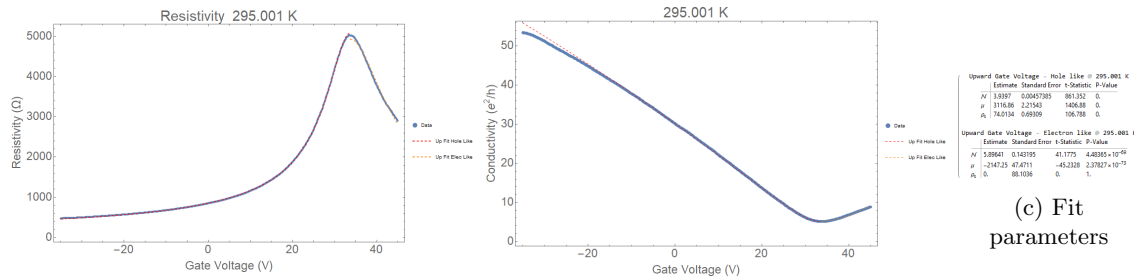
Gate dependent transport of EXF06 at 250K



(a) Resistivity fit

(b) Conductivity fit

Gate dependent transport of EXF06 at 270K



(a) Resistivity fit

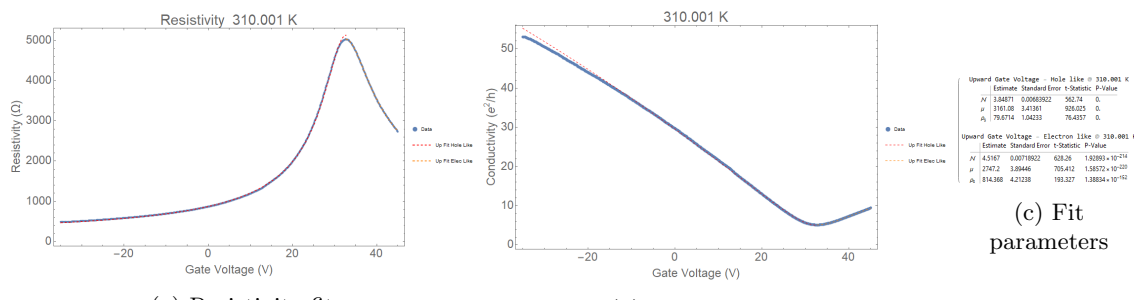
(b) Conductivity fit

(c) Fit parameters

Upward Gate Voltage	Hole like	= 295.001 K	
Estimate	StandardError	t-Statistic P-Value	
N	1.39397	0.00457895	861.352 0.
μ	319.04	2.27453	146.48 0.
ρ_1	7.63134	0.000134	596.0 0.

Upward Gate Voltage	Electron like	= 295.001 K	
Estimate	StandardError	t-Statistic P-Value	
N	5.89461	0.143919	41.1775 4.48535 $\times 10^{-49}$
μ	-2147.25	47.4711	-45.238 2.37387 $\times 10^{-12}$
ρ_2	0.	88.1036	0. t.

Gate dependent transport of EXF06 at 295K



(a) Resistivity fit

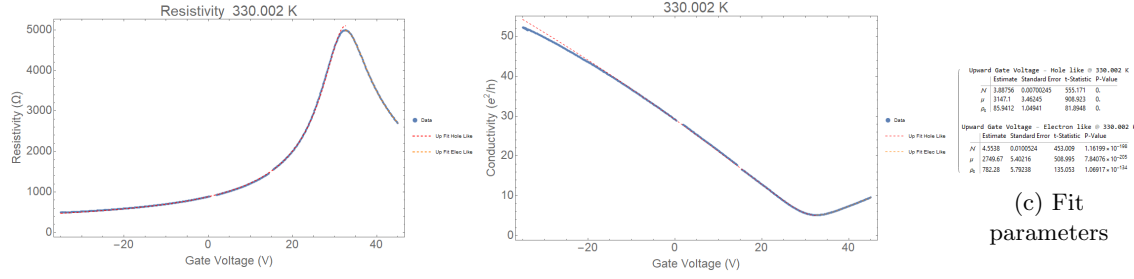
(b) Conductivity fit

(c) Fit parameters

Upward Gate Voltage	Hole like	= 310.001 K	
Estimate	StandardError	t-Statistic P-Value	
N	1.39371	0.00468002	562.74 0.
μ	310.108	2.41381	926.025 0.
ρ_1	7.95714	0.000133	764.037 0.

Upward Gate Voltage	Electron like	= 310.001 K	
Estimate	StandardError	t-Statistic P-Value	
N	4.71717	0.0700022	65.25 1.83899 $\times 10^{14}$
μ	2745.2	3.09446	705.412 1.58572 $\times 10^{-22}$
ρ_2	814.368	4.21238	193.327 1.38834 $\times 10^{-12}$

Gate dependent transport of EXF06 at 310K



(a) Resistivity fit

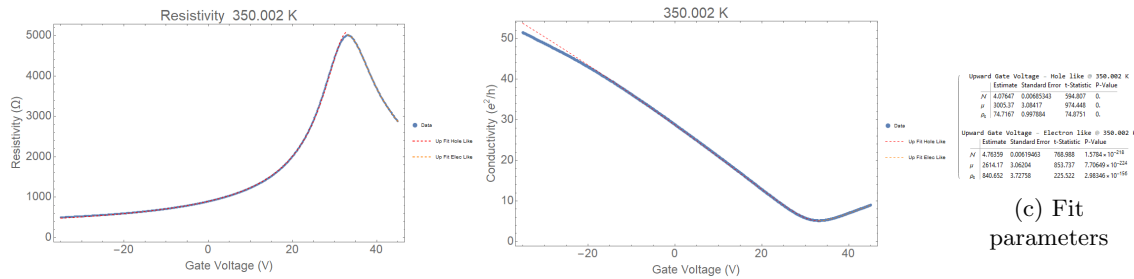
(b) Conductivity fit

(c) Fit parameters

Upward Gate Voltage	Hole like	= 330.002 K	
Estimate	StandardError	t-Statistic P-Value	
N	3.88756	0.00700245	555.171 0.
μ	319.17	2.51045	106.025 0.
ρ_1	85.8412	1.04941	81.8948 0.

Upward Gate Voltage	Electron like	= 330.002 K	
Estimate	StandardError	t-Statistic P-Value	
N	4.5538	0.0700252	403.009 1.19399 $\times 10^{-14}$
μ	2746.67	3.40216	508.995 7.84076 $\times 10^{-25}$
ρ_2	782.28	5.76238	135.053 1.04997 $\times 10^{-14}$

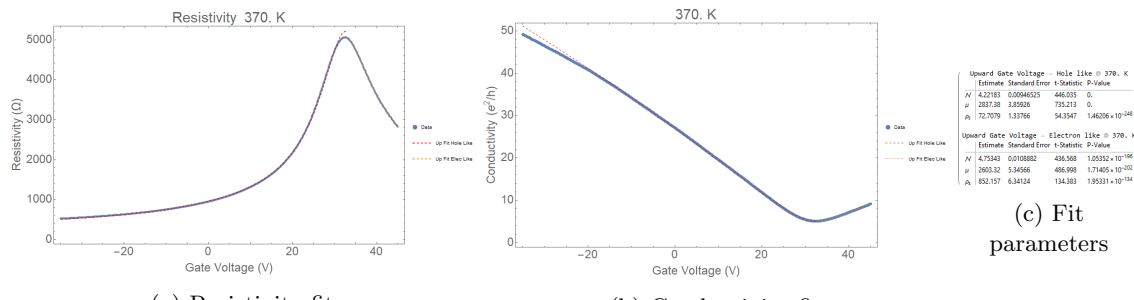
Gate dependent transport of EXF06 at 330K



(a) Resistivity fit

(b) Conductivity fit

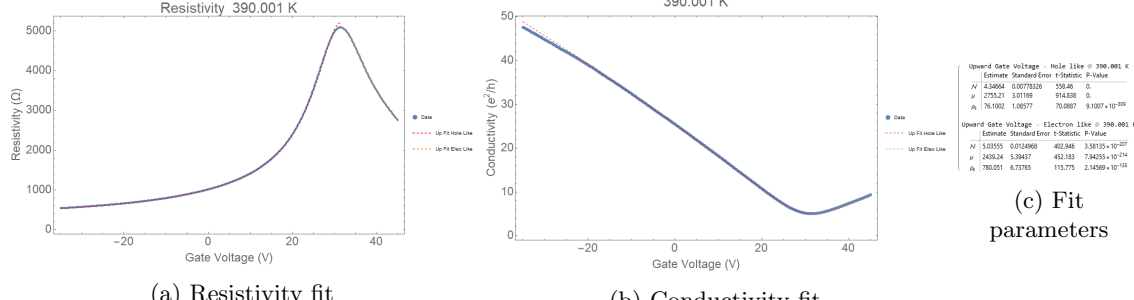
Gate dependent transport of EXF06 at 350K



(a) Resistivity fit

(b) Conductivity fit

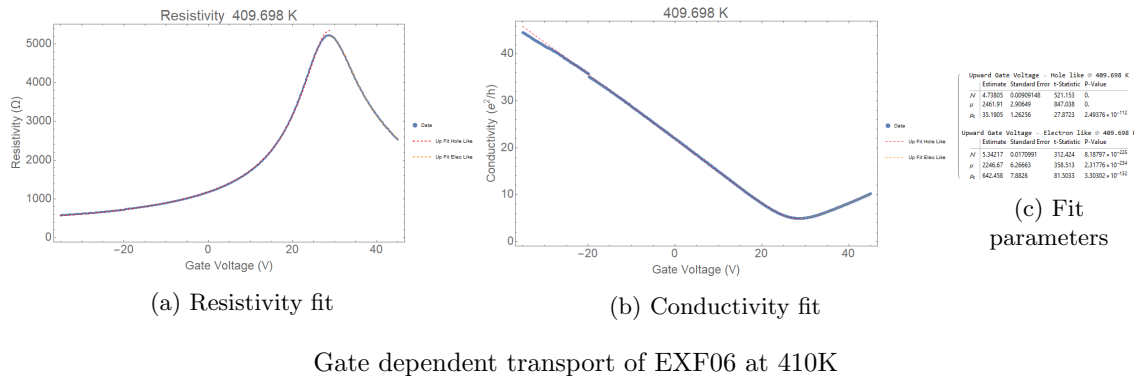
Gate dependent transport of EXF06 at 370K



(a) Resistivity fit

(b) Conductivity fit

Gate dependent transport of EXF06 at 390K



Appendix B

Theoretical electronic transport in graphene

The following set of data is generously provided by Shaffique Adam, a theoretical prediction^[39] of the transport properties of graphene for different impurity concentrations.

	n_{imp} $\times 10^{14}/\text{m}^2$	$n^*(\mathcal{N})$ $\times 10^{14}/\text{m}^2$	n_{bar}	μ m^2/Vs	σ_{\min} e^2/h
1	5	2.7159173	2.3012483	10	11.23102611
2	10	4.7817283	5.2282351	5	9.886846588
3	15	6.6227471	8.4934543	3.333333333	9.12892863
4	20	8.3359383	11.99625	2.5	8.617819538
5	25	9.9419853	15.716177	2	8.222540243
6	30	11.470562	19.61543	1.666666667	7.905627398
7	35	12.936216	23.673848	1.428571429	7.642089399
8	40	14.336173	27.901449	1.25	7.410476622
9	45	15.700392	32.244418	1.111111111	7.21391269
10	50	17.024696	36.711374	1	7.040155651
11	55	18.313618	41.294408	0.909090909	6.884689547
12	60	19.570818	45.986836	0.833333333	6.744202899
13	65	20.799315	50.782922	0.769230769	6.616199243
14	70	22.001635	55.677681	0.714285714	6.498749773
15	75	23.179922	60.666726	0.666666667	6.390334718
16	80	24.336019	65.746168	0.625	6.289736454
17	85	25.490579	70.859513	0.588235294	6.200599404
18	90	26.609358	76.101047	0.555555556	6.113146262
19	95	27.710333	81.422695	0.526315789	6.031023757
20	100	28.794599	86.821838	0.5	5.953658699
21	105	29.863135	92.29607	0.476190476	5.880564234
22	110	30.91682	97.843181	0.454545455	5.811323232
23	115	31.956449	103.46112	0.434782609	5.745576003
24	120	32.982741	109.14799	0.416666667	5.68300971
25	125	33.996354	114.90203	0.4	5.623351482
26	130	34.997886	120.72158	0.384615385	5.566360884
27	135	35.98789	126.60509	0.37037037	5.511826209
28	140	36.966872	132.55111	0.357142857	5.459559052
29	145	37.935301	138.55828	0.344827586	5.409391719

	$n_{\text{imp}} \times 10^{14} / \text{m}^2$	$n^*(\mathcal{N}) \times 10^{14} / \text{m}^2$	n_{bar}	$\mu \text{ m}^2 / \text{Vs}$	$\sigma_{\min} \text{ e}^2 / \text{h}$
30	150	38.893609	144.6253	0.333333333	5.361173775
31	155	39.842199	150.75097	0.322580645	5.31477033
32	160	40.754846	157.03654	0.3125	5.266622297
33	165	41.68318	163.28529	0.303030303	5.22335808
34	170	42.602774	169.5899	0.294117647	5.181575811
35	175	43.513933	175.94939	0.285714286	5.141184502
36	180	44.416945	182.36283	0.277777778	5.102101323
37	185	45.312079	188.82934	0.27027027	5.064250273
38	190	46.199589	195.34806	0.263157895	5.027561719
39	195	47.079714	201.91818	0.256410256	4.991971581
40	200	47.95268	208.53892	0.25	4.957420842
41	205	48.818703	215.20953	0.243902439	4.923855233
42	210	49.677984	221.9293	0.238095238	4.891224179
43	215	50.530716	228.69753	0.232555814	4.859481038
44	220	51.377081	235.51358	0.227272727	4.828582377
45	225	52.217252	242.37679	0.222222222	4.798487793
46	230	53.051397	249.28656	0.217391304	4.769159951
47	235	53.879671	256.24229	0.212765957	4.740563547
48	240	54.702224	263.24341	0.208333333	4.712665787
49	245	55.519202	270.28937	0.204081633	4.685436221
50	250	56.330739	277.37964	0.2	4.658845838
51	255	57.136969	284.51369	0.196078431	4.632867905
52	260	57.938015	291.69104	0.192307692	4.607476869
53	265	58.733999	298.9112	0.188679245	4.582649029
54	270	59.525035	306.1737	0.185185185	4.558361827
55	275	60.346963	313.29249	0.181818182	4.537280458
56	280	61.130001	320.62816	0.178571429	4.514080205
57	285	61.90845	328.0045	0.175438596	4.491361071
58	290	62.682407	335.42107	0.172413793	4.469105087
59	295	63.451968	342.87747	0.169491525	4.44729543
60	300	64.217223	350.37329	0.166666667	4.425915989
61	305	64.978261	357.90816	0.163934426	4.404951637
62	310	65.735166	365.48169	0.161290323	4.384387893
63	315	66.488021	373.09352	0.158730159	4.364211128
64	320	67.236904	380.74329	0.15625	4.344408243
65	325	67.981891	388.43065	0.153846154	4.324966816
66	330	68.723057	396.15525	0.151515152	4.305875116
67	335	69.460473	403.91677	0.149253731	4.287121867
68	340	70.194206	411.71489	0.147058824	4.26869621
69	345	70.924326	419.54928	0.144927536	4.250588099
70	350	71.650895	427.41964	0.142857143	4.232787587
71	355	72.373977	435.32567	0.14084507	4.215285404
72	360	73.093632	443.26707	0.138888889	4.198072566
73	365	73.809919	451.24355	0.136986301	4.181140524
74	370	74.522896	459.25483	0.135135135	4.164481135
75	375	75.232617	467.30064	0.133333333	4.148086472
76	380	75.939137	475.3807	0.131578947	4.131949076
77	385	76.642507	483.49475	0.12987013	4.116061664
78	390	77.342779	491.64254	0.128205128	4.100417377

	n_{imp} $\times 10^{14} / \text{m}^2$	$n^*(\mathcal{N})$ $\times 10^{14} / \text{m}^2$	n_{bar}	μ m^2 / Vs	σ_{\min} e^2 / h
79	395	78.040001	499.8238	0.126582278	4.085009495
80	400	78.734222	508.0383	0.125	4.069831687
81	405	79.425488	516.28578	0.12345679	4.054877779
82	410	80.113845	524.56601	0.12195122	4.040141899
83	415	80.799337	532.87875	0.120481928	4.02561836
84	420	81.482007	541.22378	0.119047619	4.011301694
85	425	82.161896	549.60087	0.117647059	3.997186595
86	430	82.795174	558.30549	0.11627907	3.981158491
87	435	83.468339	566.75681	0.114942529	3.967394747
88	440	84.138822	575.23981	0.113636364	3.953817784
89	445	84.80666	583.75427	0.112359551	3.940423025
90	450	85.471889	592.3	0.111111111	3.927206051
91	455	86.134546	600.87679	0.10989011	3.914162682
92	460	86.794666	609.48446	0.108695652	3.90128883
93	465	87.452283	618.1228	0.107526882	3.888580539
94	470	88.10743	626.79163	0.106382979	3.876033976
95	475	88.76014	635.49078	0.105263158	3.863645471
96	480	89.410444	644.22004	0.104166667	3.85141142
97	485	90.058374	652.97926	0.103092784	3.839328411
98	490	90.703959	661.76825	0.102040816	3.827393042
99	495	91.347231	670.58683	0.101010101	3.815602177
100	500	91.988216	679.43485	0.1	3.803952556
101	505	92.626945	688.31213	0.099009901	3.792441253
102	510	93.263445	697.21851	0.098039216	3.781065294
103	515	93.897743	706.15382	0.097087379	3.769821822
104	520	94.529865	715.11791	0.096153846	3.758708047
105	525	95.159838	724.11063	0.095238095	3.747721328
106	530	95.787687	733.13181	0.094339623	3.736859045
107	535	96.413437	742.1813	0.093457944	3.726118675
108	540	97.037112	751.25896	0.092592593	3.715497749
109	545	97.658736	760.36464	0.091743119	3.704993892
110	550	98.278333	769.49819	0.090909091	3.694604812
111	555	98.895926	778.65948	0.09009009	3.684328265
112	560	99.511537	787.84835	0.089285714	3.674162048
113	565	100.12519	797.06467	0.088495575	3.664104111
114	570	100.7369	806.3083	0.087719298	3.654152148
115	575	101.3467	815.57912	0.086956522	3.644304581
116	580	101.9546	824.87697	0.086206897	3.634559068
117	585	102.56062	834.20175	0.085470085	3.624913697
118	590	103.16479	843.55331	0.084745763	3.615366975
119	595	103.76712	852.93152	0.084033613	3.605916761
120	600	104.36764	862.33627	0.083333333	3.596561678

Table B.1: Table 1 - Theoretical values of impurities in graphene relating to other parameters.